A.L. Kachelmyer

Range-Doppler Imaging with a Laser Radar

The design of imaging waveforms for a heterodyne-detection range-Doppler laser radar depends on target dynamics as well as hardware constraints. This article describes the electric fields of the signals, the optimal form of the receiver, and the signal processing issues associated with range-Doppler imaging. The performance of unmodulated pulse trains, linear-frequency-modulated (LFM) chirp pulse trains, and biphase shift-keyed (BPSK) pulse trains as imaging waveforms is addressed. Two methods of coherent imaging are developed: one method is suitable for periodic pulse trains and the other method is a more generalized approach. Relationships between the target spin rate and the waveform parameters for unambiguous range-Doppler imaging are presented; the radar ambiguity function establishes a relative performance comparison of the waveform types. Two receiver block diagrams are presented: one specifically for processing the LFM chirp pulse train waveform and another more generalized processor for a wide variety of pulse train waveforms. Receiver signal processing issues and trade-offs, including range-Doppler coupling and waveform amplitude weighting for reduced range and Doppler sidelobes, are discussed. Firepond indoor test-range images illustrate the beneficial effects of zero padding and incoherent averaging. Finally, we present a scheme that compensates for amplitude errors and phase errors, and results in dramatically improved image quality.

Range-Doppler imaging allows for the creation of high-resolution images of long-range targets with a long-wavelength CO_2 laser radar. The Laser Radar Measurements Group at Lincoln Laboratory has built a wideband CO_2 range-Doppler imaging laser radar at the Firepond site in Westford, Mass. (Fig. 1). Many of the waveform and imaging processing techniques described in this article were developed for the Firepond system [1, 2]. Traditionally, laser imaging, which is accomplished with angle-angle intensity imaging, resolves the target by the narrow laser beam. Large receiver optics are required for angle-angle intensity imaging because the angular resolution of an image is proportional to λ/d, where λ is the laser wavelength and d is the diameter of the receiver aperture. For the angle-angle laser radar, the image cross-range resolution varies as a function of the target range. Thus, for a relatively long-wavelength CO_2 laser radar, the cross-range resolution is inadequate for long-range ballistic missile or satellite-imaging applications.

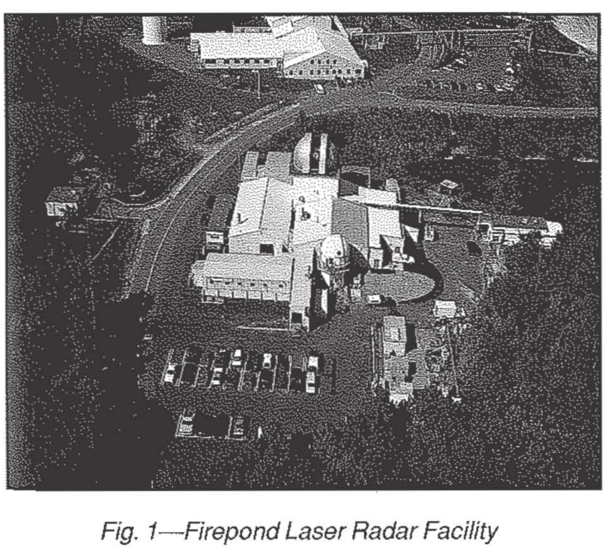

Fig. 1—Firepond Laser Radar Facility

Range-Doppler imaging with a heterodyne-detection laser radar produces high-resolution images of spinning targets; the resolution quality of the image is not determined or limited by the size of the laser radar aperture. Thus the range-Doppler laser radar does not resolve

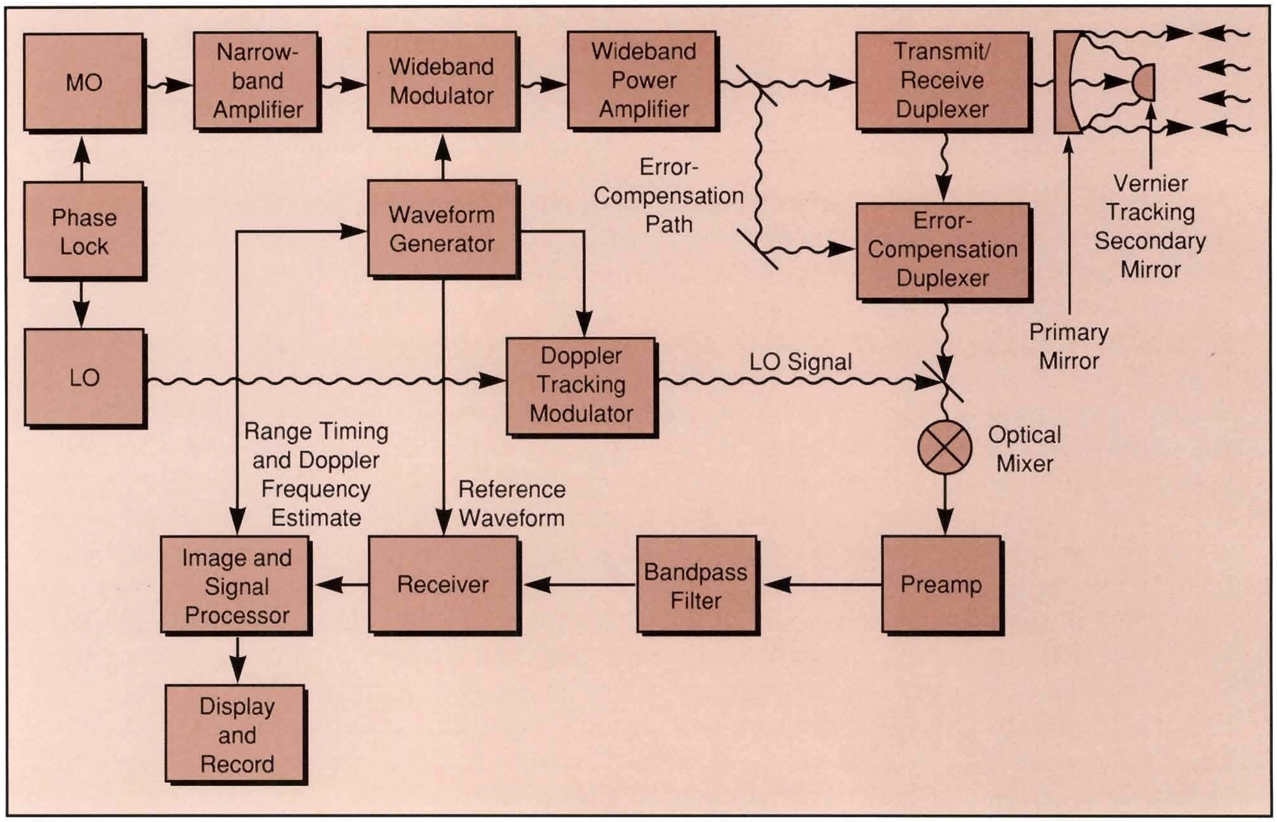

Fig. 2—Block diagram for a CO_2 laser radar system.

the target in angle with a very narrow beamwidth. Instead, the target information is derived from the coherent wideband microwave modulation imposed upon the optical carrier.

An entire image is created by capturing the return echoes from a single transmitted coherent wideband waveform. The processed target return signal is mapped into range and Doppler (cross-range) bins. The target range information is derived from the echo response of the return signal's envelope. The cross-range information is derived from the target's rotational Doppler spectrum contained within the envelope of the return signal. Range and cross-range resolution are derived respectively from the bandwidth and coherence length of the waveform.

Range-Doppler imaging is limited to targets whose rotational or vibrational motion creates measurable Doppler shifts. To determine proper cross-range scaling, target rotational rates must be known. Unresolved range and Doppler images can also be made in the multiple-target scenario in which the targets may be moving with different relative velocities but are not spinning.

The target dynamics and the desired image quality determine waveform structure, i.e., the interpulse period, the waveform coherence time, and the single-pulse bandwidth. In some situations the combination of repetitive waveforms, limited processing bandwidth, and stressing multiple-target dynamics forces the consideration of nonperiodic waveforms that require special processing techniques.

Waveform processing is addressed by first establishing the form of the matched filter (MF) receiver, given an arbitrary complex waveform envelope. The optimal form of the receiver filter is derived in terms of the transmitted waveform's complex signal envelope by maximizing the signal-to-noise ratio in the strong local oscillator (LO) signal case.

Although many potential range-Doppler imaging waveforms exist, the special properties of the linear frequency-modulated (LFM) chirp pulse train waveform and the biphase shift-keyed (BPSK) pulse train waveform are especially attractive. The advantage of the LFM chirp pulse train is that *stretch* processing (a type of correlation processing) can be used; the receiver processing bandwidth requirements are then reduced without compromising or reducing the resolution of the waveform. The constant-envelope BPSK pulse train waveform has superior resolution, low time sidelobes (without amplitude weighting), and reduced Doppler ambiguity peaks. In this article the performance of these two periodic waveforms is compared to the performance of a simple unmodulated pulse train waveform that, practically speaking, is less interesting because of its high peak-power requirements.

Coherent Range-Doppler Laser Radar

Figure 2 shows a block diagram that illustrates the major components of a coherent heterodyne range-Doppler laser radar. The master oscillator (MO) signal is amplified and fed to the wideband modulator that imposes the wideband microwave signal onto the optical MO signal. The modulated signal is then amplified by the wideband amplifier and directed out through the transmit optics to the target. Next, the Doppler-shifted target return signal is optically coaligned with a Doppler-shifted optical LO signal. The resultant optical signal is fed into a wideband optical mixer, and the heterodyne-detected intermediate frequency (IF) output is fed to the receiver. The optimal receiver forms an MF to the complex envelope of the return signal. From the processed MF outputs, range-Doppler images are created.

The optical train also includes a feedback loop for the real-time or postprocessing compensation of the amplitude and phase errors that the imperfect transmitter introduces. This feedback loop also allows for compensation of systematic receiver errors.

Transmitted/Received-Signal Field Representations

The transmitted range-Doppler waveform can be represented as a quasi-monochromatic linearly polarized electric field

$$e(\boldsymbol{\rho}, t) = \mathrm{Re}\left[\mathbf{E}_T(\boldsymbol{\rho}, t) e^{j(2\pi\nu t + kz)}\right],$$

with complex envelope

$$\mathbf{E}_T(\boldsymbol{\rho}, t) = \sqrt{\frac{2P_T}{c\varepsilon_0}}\mathbf{s}(t)\mathcal{E}_T(\boldsymbol{\rho})$$

where the time-domain complex signal envelope $\mathbf{s}(t)$ is used to create the range-Doppler image. In these equations c is the speed of light, ε_0 is the vacuum permittivity, $1/(c\varepsilon_0)$ is the impedance of free space, P_T is the average transmitted signal power, ν is the optical carrier frequency, and z is the position along the optical axis. The wave number k is defined as $2\pi/\lambda$, where λ is the wavelength of the optical carrier. The spatial variable $\boldsymbol{\rho} = (x, y)$ is the two-dimensional position vector in the exit pupil of the transmitter.

The complex signal envelope and the complex spatial electric-field pattern $\mathcal{E}_T(\boldsymbol{\rho})$ (spatial mode) are normalized to satisfy

$$\begin{aligned}\int_0^{\mathcal{T}} |\mathbf{s}(t)|^2 dt &= \mathcal{T} \\ \int_{A_T} |\mathcal{E}_T(\boldsymbol{\rho})|^2 d\boldsymbol{\rho} &= 1\end{aligned} \tag{1}$$

where $\mathcal{T}$ is the duration of the coherent waveform and A_T defines the transmitter aperture region.

The complex envelope of the electric field at the point $\boldsymbol{\rho}_0$ in the $z = R$ target plane can be described by using the extended Huygens-Fresnel diffraction integral as

$$\mathbf{E}_t(\boldsymbol{\rho}_0, t) = \int_{A_T} \mathbf{E}_T(\boldsymbol{\rho}, t - R/c)\mathbf{h}_R(\boldsymbol{\rho}_0, \boldsymbol{\rho}) d\boldsymbol{\rho}.$$

Similarly, the complex envelope of the electric field at the point $\boldsymbol{\rho}$ in the receiver entrance pupil is

$$\mathbf{E}_r(\boldsymbol{\rho}, t) = \int_{S_t} \mathbf{E}_t(\boldsymbol{\rho}_0, t - R/c)\mathbf{T}(\boldsymbol{\rho}_0)\mathbf{h}_R(\boldsymbol{\rho}_0, \boldsymbol{\rho}) d\boldsymbol{\rho}_0 \tag{2}$$

where $\mathbf{T}(\boldsymbol{\rho}_0)$ is the complex reflection coefficient of the target at the point $\boldsymbol{\rho}_0$, and the diffraction integral is taken over the target surface S_t. The

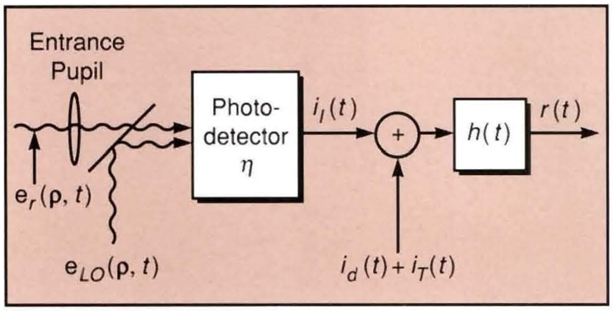

Fig. 3—Simplified heterodyne-detection system.

linear stochastic spatial atmospheric system is modeled by the Green's function as

$$\mathbf{h}_R(\boldsymbol{\rho}_0, \boldsymbol{\rho}) = \frac{1}{j\lambda R} \exp\left[jkR\left(1 + \frac{|\boldsymbol{\rho}_0 - \boldsymbol{\rho}|^2}{2R^2}\right)\right] \cdot \exp\left[\chi(\boldsymbol{\rho}_0, \boldsymbol{\rho}) + j\phi(\boldsymbol{\rho}_0, \boldsymbol{\rho}) - \frac{\alpha R}{2}\right]$$

where χ and ϕ are jointly Gaussian stochastic processes that represent the turbulence-induced log-amplitude and phase perturbations, and α is the atmospheric absorption coefficient at the transmitter wavelength [3]. Time independence is assumed in the atmospheric model in that the measurement time $\mathcal{T}$ and the round-trip propagation time $2R/c$ are less than the atmospheric coherence time. Targets with both specular (glint) and diffuse (speckle) reflection components can be modeled; $\mathbf{T}(\boldsymbol{\rho}_0)$ is deterministic for specular targets and stochastic for diffuse targets.

The electric field of the received signal plus background light is

$$e_r(\boldsymbol{\rho}, t) = \mathrm{Re}\left\{\mathbf{E}_r(\boldsymbol{\rho}, t) e^{j2\pi(\nu + f_D)t + jkz}\right\} + e_n(\boldsymbol{\rho}, t)$$

where $e_n(\boldsymbol{\rho}, t)$ represents the background-light contribution, f_D is the Doppler frequency shift introduced by the radial motion of the target (i.e., translational motion along the radar's line of sight), and $z = 0$ corresponds to the plane of the receiver entrance pupil.

The stochastic complex envelope of the return electric field can be described in terms of its normalized spatial and temporal components in the following manner:

$$\mathbf{E}_r(\boldsymbol{\rho}, t) = \sqrt{\frac{2P_s}{c\varepsilon_0}} \mathbf{s}_r(t) \mathcal{E}_r(\boldsymbol{\rho})$$

where P_s is the received signal power, and where the return signal envelope is a function of the delayed transmit envelope, i.e.,

$$\mathbf{s}_r(t) = f\left(\mathbf{s}(t - 2R/c)\right).$$

Atmospheric absorption and dispersion can drastically alter the complex envelope of the transmitted signal, especially if the target causes a large Doppler shift of the optical carrier frequency on the return path [4]. The normalizations

$$\int_0^{\mathcal{T}} |\mathbf{s}_r(t)|^2 dt = \mathcal{T}$$
$$\int_{A_r} |\mathcal{E}_r(\boldsymbol{\rho})|^2 d\boldsymbol{\rho} = 1 \qquad (3)$$

are assumed, where A_r defines the receiver aperture.

For range-Doppler imaging, an understanding of how target speckle effects are introduced into the return signals can be instructive. From Eq. 2 we see that the target speckle characteristics are imposed upon the return field envelope $\mathbf{E}_r(\boldsymbol{\rho}, t)$ by the complex reflection coefficient of the target. In a sense, the complex reflection coefficient $\mathbf{T}(\boldsymbol{\rho})$, as measured by the radar, contains all the spatial target information, while the return signal envelope $\mathbf{s}_r(t)$ contains the temporal target information, i.e., target spin and dynamics information.

Optimal Form of the Receiver

Figure 3 illustrates a basic heterodyne system configuration. In this configuration, $i_l(t)$ represents the light current that the photodetector generates, $i_d(t)$ is the dark current, and $i_T(t)$ is the thermal noise current. The thermal noise current $i_T(t)$ is a zero-mean Gaussian process of spectral height $2kT/R_L$, where kT is the thermal energy at temperature T (°K) and R_L is the effective output impedance of the photodetector. The postdetection bandpass processing is accomplished with a filter whose response is represented by $h(t)$ in the time domain. The bandpass output current, or signal, $r(t)$ is of the form

$$r(t) = \int_{-\infty}^{\infty} \{ i_l(\tau) + i_T(\tau) + i_d(\tau) \} h(t-\tau) d\tau$$

where, in the shot-noise-limited condition, the thermal and dark-current noise contributions are neglected. The choice of the complex envelope $\mathbf{h}(t)$ of the bandpass filter

$$h(t) = \mathrm{Re}\left[\mathbf{h}(t) \exp(j2\pi f_{IF} t) \right]$$

establishes the form of the range-Doppler imaging receiver and signal processor.

Maximizing the Carrier-to-Noise Ratio

The optical LO electric field can be described as

$$e_{LO}(\boldsymbol{\rho}, t) = \mathrm{Re}\left\{ \mathbf{E}_{LO}(\boldsymbol{\rho}, t) e^{j2\pi(\nu + \hat{f}_D - f_{IF})t + jkz} \right\}$$

with complex envelope

$$\mathbf{E}_{LO}(\boldsymbol{\rho}, t) = \sqrt{\frac{2P_{LO}}{c\varepsilon_0}} \mathbf{s}_{LO}(t) \mathcal{E}_{LO}(\boldsymbol{\rho})$$

where P_{LO} is the LO peak power, $\mathcal{E}_{LO}(\boldsymbol{\rho})$ is the normalized spatial field pattern of the LO signal, and $\nu + \hat{f}_D - f_{IF}$ is the LO carrier frequency. The term f_{IF} represents the desired IF after heterodyning, and $\hat{f}_D$ is the radial velocity of the target as estimated by the receiver. The quantity $\mathbf{s}_{LO}(t)$ represents the normalized amplitude and phase modulation of the optical LO signal. This generalized form of the complex envelope of the electric field allows for return-signal preconditioning by the optical LO signal.

The antenna theorem for heterodyne reception [5] allows us to treat the LO electric field $e_{LO}(\boldsymbol{\rho}, t)$ as if it were present in the receiver's entrance pupil, and to perform the heterodyne mixing calculation in the receiver's entrance-pupil plane. The mean Poisson light current out of the photomixer is proportional to the integral of the incident electric-field intensity (modulus squared of the complex envelope) over the receiver aperture [6], or the Poisson rate function. The conditional mean Poisson light current, given the Poisson rate function, is

$$\begin{aligned} \bar{i}_l(t) &= \frac{qG\eta c\varepsilon_0}{2h\nu} \int_{A_r} \left| \mathbf{E}_r(\boldsymbol{\rho}, t) + \mathbf{E}_{LO}(\boldsymbol{\rho}, t) \right|^2 d\boldsymbol{\rho} \\ &\approx \mathrm{Re}\left[\mathbf{y}_{IF}(t) \exp(j2\pi f_{IF} t) \right] + n_{LO}(t) \end{aligned}$$

where the complex envelope of the bandpass target return-signal contribution is

$$\begin{aligned} \mathbf{y}_{IF}(t) = \frac{qG\eta}{h\nu} \sqrt{P_s P_{LO}}\, \mathbf{s}_r(t) \mathbf{s}^*_{LO}(t) e^{j\Phi} \cdot \\ \int_{A_r} \mathcal{E}_r(\boldsymbol{\rho}) \mathcal{E}^*_{LO}(\boldsymbol{\rho}) d\boldsymbol{\rho} \end{aligned} \tag{4}$$

and where the dominant LO shot-noise contribution (the return signal and background shot noise are negligible compared to the LO shot noise) is given by

$$n_{LO}(t) = \frac{qG\eta P_{LO}}{2h\nu} \left| \mathbf{s}_{LO}(t) \right|^2 \int_{A_r} \left| \mathcal{E}_{LO}(\boldsymbol{\rho}) \right|^2 d\boldsymbol{\rho}.$$

In the above equations η is the quantum efficiency of the photodetector, $h\nu$ is the amount of energy per photon, ν is the optical carrier frequency, h is Planck's constant, q is the electron charge, and G is the nonrandom gain of the photodetector.

We assume that the estimate of target radial velocity by the receiver is perfect ($\hat{f}_D = f_D$), the background-noise contribution is negligible, and bandpass filtering removes the signal components that fall out of the IF passband. The phase term Φ in Eq. 4 accounts for the relative timing and path-length differences between the return and the LO electric fields. In general the target return undergoes Doppler shift and varies in range from return to return. Even if the target-return Doppler shift could be estimated perfectly, the unknown phase difference would still remain.

The bandpass process $r(t)$ is of the form

$$r(t) = \mathrm{Re}\left[\mathbf{r}(t) \exp(j2\pi f_{IF} t) \right] \tag{5}$$

with complex envelope

$$\mathbf{r}(t) = \mathbf{y}(t) + \mathbf{n}(t).$$

The conditional mean of the complex signal process is given by

$$\bar{\mathbf{y}}(t) = \int_{-\infty}^{\infty} \mathbf{y}_{IF}(\tau)\mathbf{h}(t-\tau)\,d\tau.$$

The mean Poisson signal process $\bar{\mathbf{y}}(t)$ is stochastic, because the received signal power P_s is a random variable due to atmospheric turbulence and target speckle.

The variance of the complex noise process is

$$\mathrm{var}\{\mathbf{n}(t)\} = qG\int_{-\infty}^{\infty} n_{LO}(\tau)|\mathbf{h}(t-\tau)|^2\,d\tau.$$

In general, $\mathbf{n}(t)$ represents the complex envelope of the noise process, which includes contributions from the LO shot noise, signal shot noise, thermal noise, background light, and dark current. In the strong LO condition, the high-density LO shot makes $\mathbf{n}(t)$ a circulo-complex Gaussian noise process.

The carrier-to-noise ratio (CNR) is defined as

$$\mathrm{CNR} \equiv \frac{\mathrm{E}|\bar{\mathbf{y}}(t)|^2}{\mathrm{var}\{\mathbf{n}(t)\}}.$$

The Schwarz inequality is applied twice to maximize the CNR with respect to both the bandpass filter complex envelope and the LO field pattern. This method yields the optimal forms

$$\mathbf{h}(t) = \frac{\mathbf{s}_r^*(t_0 - t)}{\mathbf{s}_{LO}^*(t_0 - t)}$$

$$\mathcal{E}_{LO}(\boldsymbol{\rho}) = \mathcal{E}_r(\boldsymbol{\rho})$$

where t_0 is a constant delay term needed to make the filter physically realizable, or causal. The complex envelope of the LO signal augments the optimal filter. However, the relative timing between the return and LO envelopes may have to be tightly controlled when the LO envelope represents a wideband pulsed modulation.

Both the temporal and spatial complex-envelope solutions can be generalized by including a constant phase term, without affecting the CNR. When we apply the idealized spatial and time-domain MF solutions, the CNR at the output of the bandpass filter becomes

$$\mathrm{CNR} = \frac{\eta \bar{P}_s \mathcal{T}}{h\nu}$$

using the normalizations defined by Eq. 3 and where $\bar{P}_s$ is the average return signal power. The CNR can be expressed in the form of the monostatic radar equation [7] for an unresolved target at range R as

$$\mathrm{CNR} = \frac{\eta P_T \mathcal{T}}{h\nu}\,\frac{G_T}{4\pi R^2}\,\frac{\sigma A_r}{4\pi R^2}\,\varepsilon_{opt}\,\varepsilon_{het}\,e^{-2\alpha R} \quad (6)$$

where η is the photodetector's quantum efficiency, $h\nu$ is the photon energy, $P_T\mathcal{T}$ is the energy in the transmitted waveform, G_T is the transmitter antenna (telescope) gain, σ is the radar cross section of the target, A_r is the receiver area, ε_{opt} is the optical efficiency of the transmitter and receiver, ε_{het} is the heterodyne mixing efficiency, and α is the atmospheric extinction coefficient. For a circular transmitter aperture of diameter d, the receiver area is $A_r = \pi d^2/4$ and the telescope's far-field pattern (Airy pattern) gain is $G_T = \pi^2 d^2/\lambda^2$. For a speckle target the radar cross section is $\sigma = 4\rho A_t$, where ρ is the speckle-target diffuse reflectivity and A_t is the cross-sectional area of the target as seen from the radar's viewing angle.

Equation 6 is the *quantum-limited* CNR, which is valid under the assumption that the LO shot noise greatly exceeds the thermal Gaussian noise, the background-light shot noise, and the dark-current shot noise. The form of the optimal bandpass filter justifies the underlying premise of the waveform processing methods, which is to perform temporal matched filtering of the transmitted waveforms.

Image SNR

Equation 2 shows that the complex envelope of the return electric field is a stochastic process. The complex envelope out of the bandpass MF from Eq. 5, sampled at the peak output time, can be modeled in the normalized form

$$\mathbf{r} = \mathbf{y} + \mathbf{n}$$

with a signal contribution

$$\mathbf{y} = \sqrt{\frac{\eta P_T \mathcal{T}}{h\nu}} \int_{S_t} \mathcal{E}_t^2(\boldsymbol{\rho})\mathbf{T}(\boldsymbol{\rho})\cdot \exp\left[2\chi(\boldsymbol{\rho},0) + 2j\phi(\boldsymbol{\rho},0) - \alpha R\right]d\boldsymbol{\rho},$$

and where $\mathbf{n}$ is a unit-variance zero-mean complex Gaussian random variable [3]. The free-space radar beam pattern $\mathcal{E}_t(\boldsymbol{\rho})$ in the target plane is produced by the transmitted spatial mode $\mathcal{E}_T(\boldsymbol{\rho})$.

The LO spatial beam pattern is matched to the transmitted beam pattern $\mathcal{E}_{LO} = \mathcal{E}_T^*$, and a monostatic radar configuration with a shared aperture is assumed. The turbulence log-amplitude and phase parameters $\chi(\boldsymbol{\rho},\mathbf{0})$ and $\phi(\boldsymbol{\rho},\mathbf{0})$ are referenced to the center of the receiver aperture ($\boldsymbol{\rho}_r = \mathbf{0}$) under the assumption that the coherence length of the turbulence is much greater than the diameter d of the aperture. In the turbulence-free case, the aperture-averaged complex reflection coefficient of the target controls the statistics of the MF output; the MF output is a circulo-complex Gaussian random process. Atmospheric turbulence induces additional log-normal amplitude scintillation and phase fluctuation of the complex envelope of the MF output.

The image signal-to-noise ratio (SNR) is defined as

$$\mathrm{SNR} \equiv \frac{\left(\mathrm{E}|\mathbf{y}|^2\right)^2}{\mathrm{var}\left\{|\mathbf{r}|^2\right\}}.$$

Shapiro [3] has shown that

$$\mathrm{SNR} = \frac{\dfrac{\mathrm{CNR}}{2}}{1 + \dfrac{\mathrm{CNR}}{2\mathrm{SNR}_{sat}} + \dfrac{1}{2\mathrm{CNR}}}$$

where the saturation SNR is

$$\mathrm{SNR}_{sat} \equiv \frac{\left(\mathrm{E}|\mathbf{y}|^2\right)^2}{\mathrm{var}\left(|\mathbf{y}|^2\right)}.$$

The saturation SNR accounts for fluctuations that are entirely due to target speckle or turbulence scintillation in the return signal.

In Fig. 4, the saturation SNR is plotted for the speckle and glint target cases versus the turbulence variance parameter σ_x^2. The corresponding image SNR for a CNR of 10 dB is also plotted for both cases. For simplicity, the turbulence log-amplitude aperture averaging factor is assumed to be unity, which represents the worst-case fluctuation (see Ref. 3 for more details). Figure 4 shows that the best image SNR in the high-CNR and low-turbulence regime for speckle targets is SNR = 1.

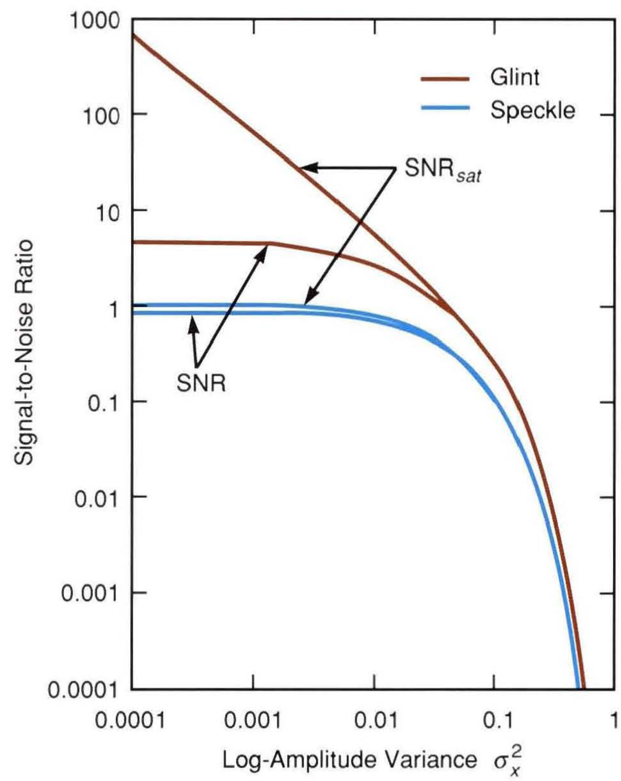

Fig. 4—Saturation SNR and image SNR with CNR = 10, for both glint and speckle targets as a function of the log-amplitude variance of the turbulence.

Incoherent averaging can raise the image SNR if the radar PRF is large enough to prevent target-image smearing. With perfect alignment of the image pixels, the image SNR after averaging l frames, or images, is

$$\mathrm{SNR}(l) = l \cdot \mathrm{SNR}.$$

Range-Doppler Imaging

Range-Doppler images are created by taking advantage of the rotational motion of the targets. This rotational motion gives rise to a rotational Doppler spectrum in the target return waveform, which is processed to produce an image. Similarly, the relative motion and range separation between multiple unresolved targets can be used to create a range-Doppler map of the target space. In addition, the Doppler frequency shift of the target return due to radial motion can be used to make precision velocity measurements.

The coherent target return envelopes produce the range-Doppler images. Each image pixel is viewed as the response of an MF that is adjusted to that pixel's range and Doppler coordinate. The waveforms are represented in terms of their complex envelopes in the pulse train format

$$\mathbf{s}(t) = \sum_{k=0}^{N_p - 1} \mathbf{p}(t - kT_s) \tag{7}$$

where N_p is the number of pulses in the train, and T_s is the interpulse spacing, or pulse period. The single-pulse envelope is defined in terms of its real-valued amplitude $a(t)$ and phase $\phi(t)$ functions as

$$\mathbf{p}(t) = a(t)e^{j\phi(t)}.$$

The return envelope can be coherently processed in two fundamental ways:

Ambiguity-function-like (AFL) images are formed from a two-dimensional MF (range and Doppler) to the entire return waveform envelope.

Subaperture-ambiguity-function-like (SAFL) images are produced by first forming a single-pulse MF to the return pulse train envelope. Then the image range dimension is formed from this periodic MF output (the range response is repeated for each return pulse), and the image Doppler or cross-range dimension is formed from the pulse-to-pulse variation of the periodic MF output.

SAFL images are formed with pulse train waveforms with $N_p >> 1$, while AFL images are formed with single-pulse nonperiodic waveforms where $N_p = 1$ or with waveforms where N_p is small.

The SAFL imaging method, which is designed for periodic pulse train waveforms, requires fewer computations because of its reduced range and Doppler window (subaperture in range-Doppler space), but it also has potential range and Doppler ambiguities. The AFL imaging method has a larger range and Doppler window with greater associated computational requirements; it works equally well with nonperiodic and periodic waveforms. Figure 5 illustrates the two imaging regions (see Ref. 8 for discussions of alternate tomographic imaging methods).

Matched Filtering and the Range-Doppler Ambiguity Function

The output $\mathbf{y}_s(t)$ of a linear filter that is matched to the Doppler-shifted input signal envelope $\mathbf{s}(t)$ is

$$\mathbf{y}_s(t, \phi) = \int_{-\infty}^{\infty} \mathbf{s}(\lambda)\mathbf{s}^*(\lambda - t)e^{-j2\pi\phi\lambda}d\lambda \tag{8}$$

where ϕ is the relative frequency difference be-

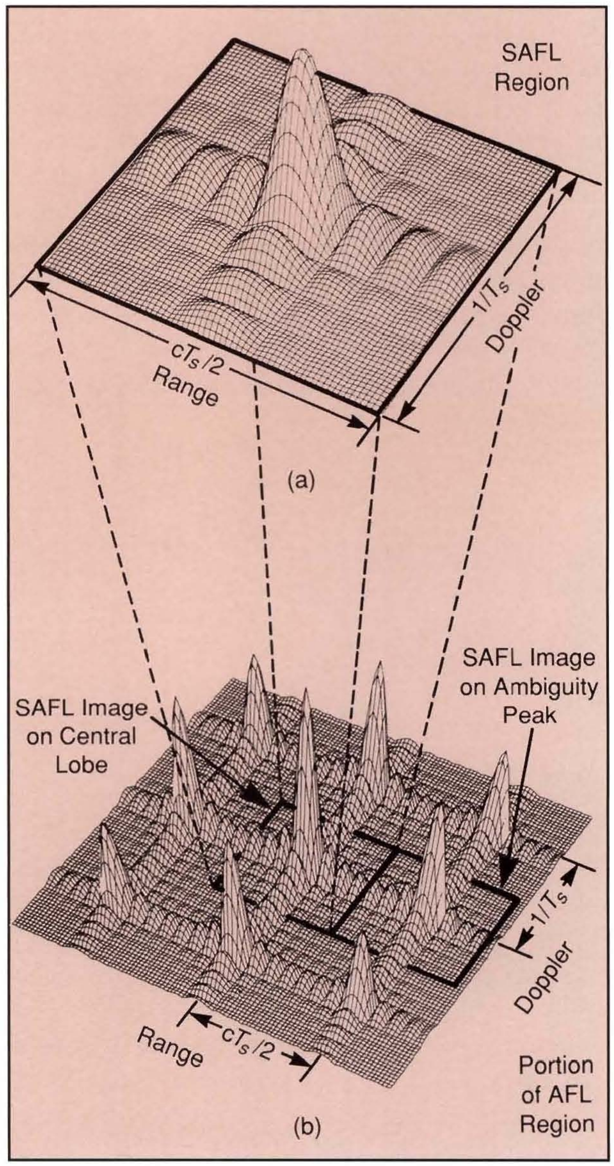

Fig. 5—(a) Subaperture-ambiguity-function-like (SAFL) and (b) ambiguity-function-like (AFL) imaging regions for a periodic waveform. The point-target response of the SAFL image is given by the central-lobe region of the point-target response of the AFL image.

tween the filter and the input. By adjusting ϕ, the filter maximizes its response to inputs with the same relative Doppler frequency shift. The MF output is a function of relative time delay; the causality condition is not violated. The MF output $\mathbf{y}_s$ and the range-Doppler ambiguity function χ_s are equivalent [9], i.e.,

$$\mathbf{y}_s(t,\phi) = \chi_s(-t,\phi).$$

The ambiguity function can be viewed as the correlation between the Doppler-shifted point-target return envelope and the transmitted signal envelope. The resolution, ambiguities, and sidelobe levels associated with the ambiguity function determine the quality of the waveform.

Ambiguity-Function-Like Images

An AFL range-Doppler image is created by forming a two-dimensional MF to the complete transmitted waveform. This waveform can be either periodic or nonperiodic. This process is accomplished in hardware by forming a bank of MFs, in which each filter is tuned to a specific frequency relative to the expected IF carrier frequency. If the target return signal envelope is sampled and recorded, then the MF bank can be implemented in software.

The complex MF output from Eq. 8, with relative frequency offset n/NT, is sampled every T seconds to form the nth row (range slice) of the range-Doppler image. The $M \times N$ intensity image for a point-target return $\mathbf{s}(t)$ at relative range $c\tau_0/2$ and Doppler frequency shift ϕ_0 is

$$I\left(iT,\frac{n}{NT}\right) = \left|\chi_s\left(\tau_0 - iT,\frac{n}{NT} - \phi_0\right)\right|^2$$
$$i = -\mathrm{int}\,[M/2],\ldots,0,\ldots,M - \mathrm{int}\,[M/2]-1,$$
$$n = -\mathrm{int}\,[N/2],\ldots,0,\ldots,N - \mathrm{int}\,[N/2]-1$$

where iT is the ith range bin and n/NT is the nth Doppler bin. The notation int [ ] indicates the integer part of the argument. When M and N are odd, the image has an equal number of bins on either side of the zero-range zero-Doppler center bin. The range and Doppler (velocity) bin sizes are $cT/2$ and $\lambda/2NT$, respectively. To satisfy Nyquist's sampling theorem, the complex sampling rate must be greater than or equal to the waveform bandwidth, i.e., $1/T \geq B$. To make the image Doppler resolution at least as good as the waveform resolution, we require that $NT \geq N_p T_s$. The point-target AFL image is just the sampled ambiguity function centered on the target range and Doppler coordinates.

SAFL Range-Doppler Images

An SAFL range-Doppler image is created by first forming a single-pulse MF to the return pulse train. The periodic single-pulse MF output is sampled and realigned in time (modulo the pulse period), and then Fourier transformed along each fixed relative range bin. The periodic single-pulse MF response for a point-target return $\mathbf{s}(t)$ at relative range $c\tau_0/2$ and Doppler frequency shift ϕ_0 becomes

$$\begin{aligned}\mathbf{y}(t;\tau_0,\phi_0) &= \int_{-\infty}^{\infty} \mathbf{s}(\lambda-\tau_0)\mathbf{p}^*(\lambda-t)e^{j2\pi\phi_0\lambda}d\lambda \\ &= e^{j2\pi\phi_0\tau_0}\sum_{k=0}^{N_p-1} e^{j2\pi\phi_0 kT_s}\chi_p(kT_s+\tau_0-t,-\phi_0)\end{aligned} \qquad (9)$$

where $\chi_p(\tau,\phi)$ is the ambiguity function of the single-pulse complex envelope $\mathbf{p}(t)$. The single-pulse MF response is sampled every T seconds, and M complex samples occur every pulse period so that $MT = T_s$. The single-pulse MF output is realigned in time so that the contribution from all N_p of the pulses at the same relative range (time) iT form the input sequence to a discrete Fourier transform (DFT). The point-target SAFL intensity image becomes

$$\begin{aligned}I\left(iT,\frac{n}{NT_s}\right) &= \left|\sum_{k=0}^{N_p-1}\mathbf{y}(kT_s+iT;\tau_0,\phi_0)e^{-j2\pi kn/N}\right|^2 \\ &= \left|\chi_p(\tau_0-iT,-\phi_0)\right|^2 \cdot \\ &\quad \left|\frac{\sin[\pi N_p(\phi_0 T_s - n/N)]}{\sin[\pi(\phi_0 T_s - n/N)]}\right|^2 \\ &\quad i = -\mathrm{int}\,[M/2],\ldots,0,\ldots,M-\mathrm{int}\,[M/2]-1 \\ &\quad n = 0,1,\ldots,N-1.\end{aligned} \qquad (10)$$

The single-pulse ambiguity-function form of the SAFL image in Eq. 10 is exact for $T_p \leq T_s/2$, where T_p is the single-pulse duration. When $T_p > T_s/2$ (and $T_p \le T_s$), Eq. 10 must use a periodic form of the single-pulse ambiguity function, and the final form of the SAFL image is an approximation, because of the finite pulse train length. The peak range response occurs in the range bin $iT = \tau_0$, and the maximum Doppler response occurs when $n/NT_s = \phi_0$. The center zero-range bin corresponds to $i = 0$ with in-range bins for $i < 0$ and where the range bin size is $cT/2$. An end-around shift of $N/2$ pixels in the Doppler dimension places the zero-Doppler pixel in the center of the image. If $\phi_0 \ge 1/T_s$ or $\tau_0 \ge T_s$, then the SAFL image lies on an ambiguity in the range-Doppler plane. For Doppler image resolution that is better than the waveform resolution, the input sequence can be zero padded with $N > N_p$. To satisfy Nyquist's sampling theorem, we require $T \le 1/B$ where B is the single-pulse bandwidth.

The SAFL image response for a point target described by Eq. 10 is determined by a single-pulse ambiguity function that is modulated by the periodic ratio of sine functions in the Doppler dimension; this point-target image response is equivalent to the central-lobe region of the periodic imaging waveform's ambiguity function (see Fig. 5). The single-pulse bandwidth determines the range resolution while the coherence length of the pulse train determines the Doppler resolution. In practice, an SAFL image is composed of the superposition of many point-target returns, each with a specific relative range and Doppler shift.

Range-Doppler Waveforms

The range-Doppler waveform parameters are chosen to provide a suitable match to the desired image or measurement criteria, the target dynamics, and the available laser radar technology. Equation 7 gives the general form of a periodic pulse train waveform. The single-pulse envelopes for three specific waveform types are defined below. In these three representations the rectangle function is defined as

$$\operatorname{rect}\left(\frac{t}{T}\right) = \begin{cases} 1 & 0 \le t < T \\ 0 & \text{otherwise} \end{cases}$$

Unmodulated pulse train. The amplitude and phase functions for a single unmodulated pulse are

$$a(t) = a_0 \operatorname{rect}\left(\frac{t}{T_p}\right)$$

$$\phi(t) = \phi_c$$

where T_p is the pulse duration and ϕ_c is an arbitrary constant phase. To satisfy Eq. 1 the constant pulse amplitude is given by $a_0 = \sqrt{T_s/T_p}$. In general, a_0 can have slow time variations with little impact on the waveform performance (for example, finite-bandwidth rounded-pulse shapes). For the simple unmodulated pulse train waveform, the time-bandwidth (TB) product increases as T_p is made smaller with respect to T_s. In fact, we define the single-pulse TB product, with respect to the interpulse spacing, to be T_s/T_p, where the single-pulse bandwidth is $1/T_p$. The pulse train TB product is therefore N_pT_s/T_p. Figure 6(a) shows an example of an unmodulated pulse train waveform.

Linear frequency-modulated (LFM) chirp pulse train. The amplitude and phase functions for a single LFM chirp pulse are

$$a(t) = a_0 \operatorname{rect}\left(\frac{t}{T_p}\right)$$

$$\phi(t) = \pi \gamma t^2$$

where γ is the chirp pulse frequency slope in Hertz per second. By definition, the chirp pulse phase is reinitialized to zero at the beginning of each chirp pulse. If this waveform is modulated onto an optical carrier of frequency υ, then each pulse period of the resulting signal will vary linearly in frequency from υ to $\upsilon + \gamma T_p$, where $B = \gamma T_p$ is the bandwidth of the chirp pulse. Also, the single-pulse TB product is $\gamma T_p T_s$ and the pulse train TB product is $N_p \gamma T_p T_s$. Figure 6(b) shows an example of an LFM chirp train waveform. The peak power requirement is minimized when the pulse width T_p equals the pulse period T_s, and the timing accuracy requirement for stretch processing is less critical.

Biphase shift-keyed (BPSK) pulse train. The amplitude and phase functions for a single

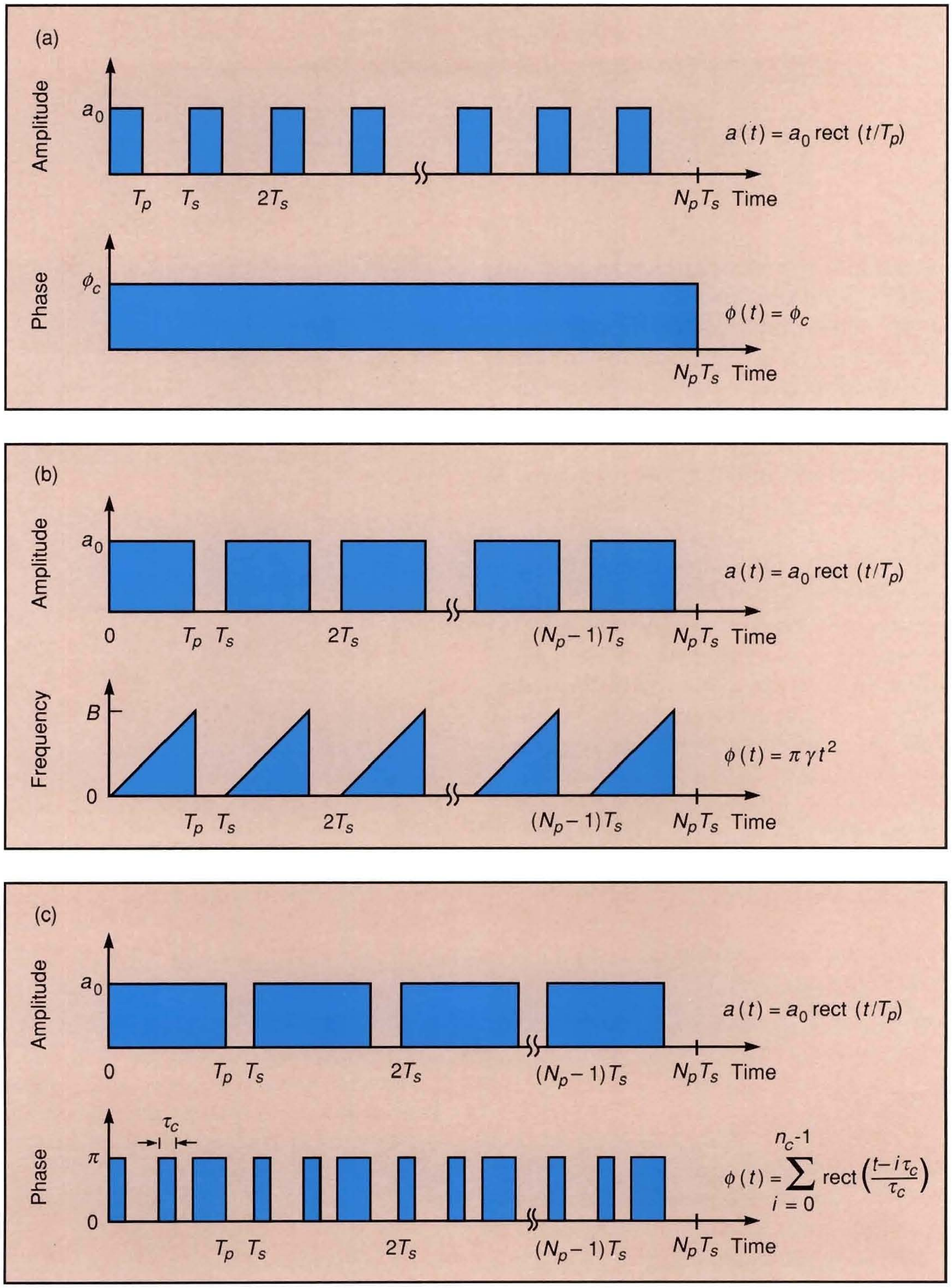

Fig. 6—The three basic waveforms: (a) Simple unmodulated pulse train waveform, (b) LFM chirp pulse train waveform, and (c) BPSK pulse train waveform.

BPSK pulse are

$$a(t) = a_0 \operatorname{rect}\left(\frac{t}{T_p}\right)$$

$$\phi(t) = \sum_{l=0}^{n_c-1} \pi b_l \operatorname{rect}\left(\frac{t - l\tau_c}{\tau_c}\right)$$

where preferably $T_s = T_p$ and where $b_l \in \{0, 1\}$ is a binary variable representing the lth bit of the pseudorandom or maximal-length code that defines the phase modulation. By definition, each bit operates on a given chip of the waveform. The chipping rate of the biphase modulation is $1/\tau_c$ where τ_c is the chip duration. There are n_c chips per pulse, i.e., $n_c\tau_c = T_p$. By definition, the TB product of the BPSK waveform is $N_p n_c T_s/T_p$ where $n_c T_s/T_p$ is the TB product of each pulse.

Maximal-length sequences are generated from linear-feedback shift registers. A q-stage shift register generates a maximal-length sequence when it passes through all possible states in a single period with sequence length $n_c = 2^q - 1$. The autocorrelation function magnitude of a periodic maximal-length sequence is two-valued; its height is n_c at shifts of ln_c, where l is an integer, and 1 for all other shifts. Figure 6(c) shows an example of a BPSK pulse train waveform based on a maximal-length sequence of length 7.

Relationship between Waveform and Target Parameters

The cross-range resolution b of a rotating target of maximum radius r_t is

$$b = \frac{2r_t}{N_t}$$

where N_t is the number of cross-range resolution cells that the target occupies in the range-Doppler image. The maximum target radius is specified because the target may have a varying radius along the spin axis. The number of cross-range target cells is defined by the ratio

$$N_t \equiv \frac{f_m}{1/\mathcal{T}}$$

where f_m is the maximum Doppler frequency extent and $1/\mathcal{T}$ is the coherence time bandwidth of the waveform, as illustrated in Fig. 7.

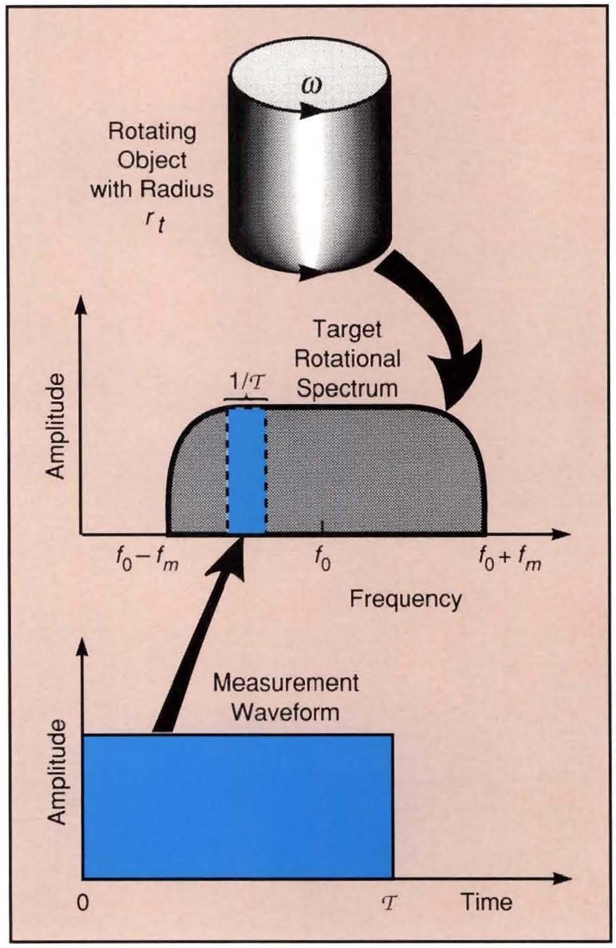

Fig. 7—Cross-range resolution. The rotating object produces a rotational spectrum of width $2f_m$ in the return waveform, where f_m is the maximum Doppler frequency. The processor divides the rotational spectrum into slices of width $1/\mathcal{T}$, where $\mathcal{T}$ is the coherence time of the measurement waveform.

For an arbitrary target with angular rotational rate ω and with waveform coherence time $\mathcal{T}$, the number of cross-range target cells is given by

$$N_t = \frac{4\omega r_t |\sin\beta| / \lambda}{1/\mathcal{T}}$$

where β is the angle between the target spin axis and the laser radar line of sight to the target. Thus the cross-range resolution of the target is

$$b = \frac{\lambda}{2\omega\mathcal{T}|\sin\beta|} \tag{11}$$

where ω is in units of radians per second. Figure 8 shows the cross-range resolution as a function of the target spin rate for a family of waveform coherence times. For a given cross-range resolution requirement, the curves show the target spin rate that is necessary to make the measurement in a given amount of time. In terms of target identification, the waveform coherence time $\mathcal{T}$ limits the set of spinning targets that can be imaged with sufficient cross-range resolution.

Target Coherence Time and Cross-Range Resolution

Target dynamics and hardware or technology constraints place limitations on the available coherent processing time $\mathcal{T}$. For rotating targets, the target limitation is the target smearing time T_{sm}. Smearing is defined to occur when the target rotates from its position at initial contact with the range-Doppler waveform by one-half of a cross-range resolution cell $b/2$. The target-smearing time relation is

$$T_{sm} = \frac{b}{2\omega r_t |\sin\beta|}.$$

If we use Eq. 11 and assume that the waveform coherence time is not limited by hardware constraints, the maximum coherence time occurs when

$$T_{sm} = \mathcal{T} = \frac{\sqrt{\lambda / r_t}}{2\omega|\sin\beta|}.$$

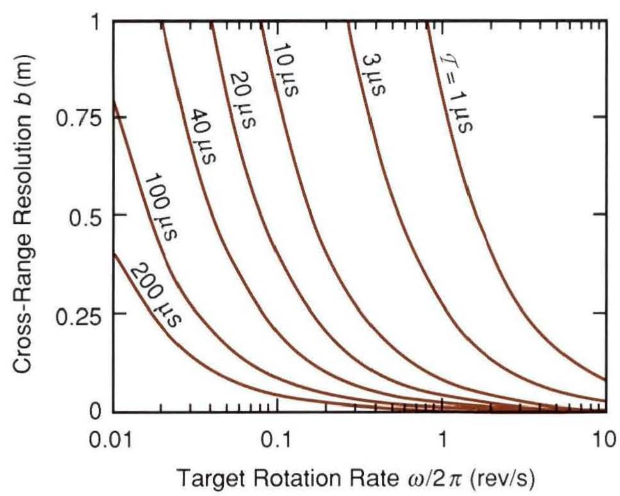

Fig. 8—Cross-range resolution versus target rotation rate for different values of the waveform coherence time $\mathcal{T}$.

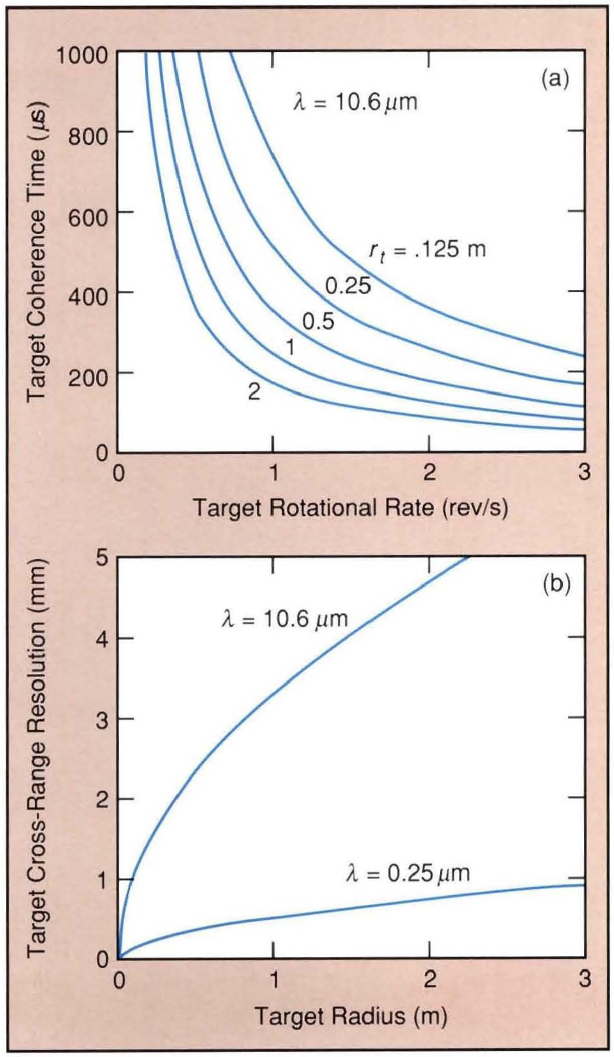

Fig. 9—(a) Maximum target coherence time versus target rotational rate, and (b) maximum target cross-range resolution versus target radius.

Figure 9(a) shows the maximum target coherence time for five values of target radius.

The best obtainable cross-range resolution b_0, under the maximum coherence time condition, is

$$b_0 = \sqrt{\lambda r_t}.$$

Figure 9(b) shows the best cross-range resolution as a function of target radius. Clearly, the optical wavelength λ sets the limit on cross-range resolution when the waveform coherence time is equal to the target smearing time. Remember that these results assume no knowledge of the target dynamics; if the target dynamics are known, then greater coherence

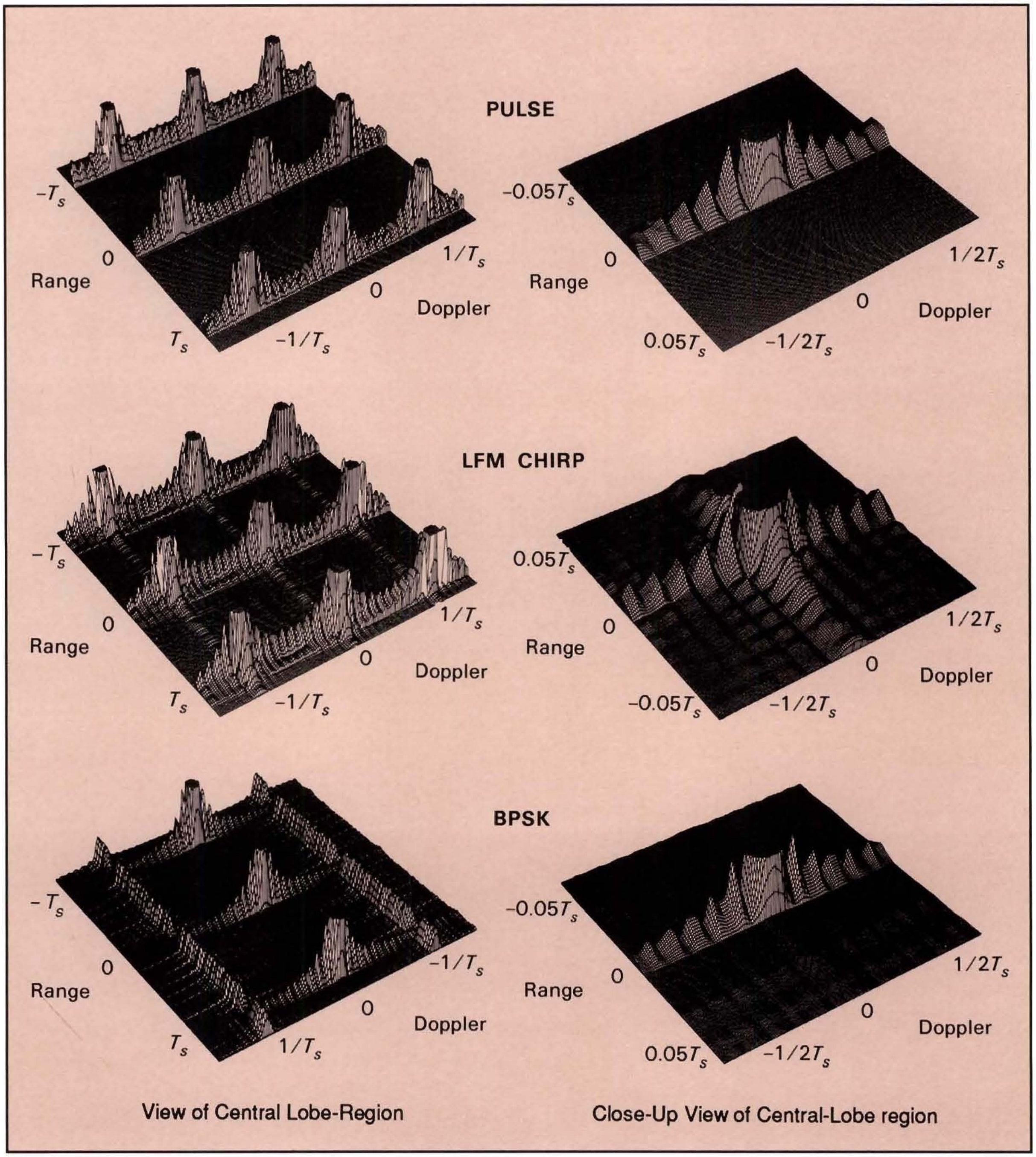

Fig. 10—Range-Doppler ambiguity functions for a 12-pulse train for each of the three waveforms. Each waveform has a single-pulse TB product of 127, and a corresponding pulse train TB product of 1524. Responses are truncated at 20% of the mainlobe peak value.

times and better resolution can be achieved.

Waveform Resolution

The range resolution of the pulse train waveforms is given by their single-pulse range resolution. The range resolution of each of the three pulse train types is

$$R_{res} = \frac{cp}{2}$$

where $p = T_p$ for the simple unmodulated pulse train, $p = \tau_c$ for the BPSK pulse train, and

$p = 1/B$ for the LFM chirp pulse (c is the speed of light and B is the chirp pulse bandwidth).

The coherent waveform duration $\mathcal{T} = NT_s$ provides a potential Doppler frequency resolution of $1/\mathcal{T}$, while the velocity resolution is

$$V_{res} = \frac{\lambda}{2\mathcal{T}}$$

where λ is the wavelength of the optical carrier.

Waveform Ambiguities

The interpulse spacing T_s generally provides a trade-off between range and Doppler ambiguities. The unambiguous range window for each of the pulse train waveforms is given by

$$R_{amb} = \frac{cT_s}{2}.$$

A target at relative range R from the center range bin must satisfy $|R| < R_{amb}/2$ to remain in the unambiguous range window.

The ambiguous Doppler frequency of each waveform equals its interpulse repetition frequency. Conceptually, each pulse in the coherent pulse train waveform forms a sample of the Doppler spectrum of the target. Therefore, the interpulse repetition frequency of the waveform is the Doppler sampling rate. By Nyquist's sampling theorem, the sampling rate must be greater than twice the maximum frequency of the target's Doppler spectrum to avoid aliasing. This restriction establishes the ambiguous Doppler frequency $1/T_s$ in terms of the ambiguous velocity V_{amb} as

$$V_{amb} = \frac{\lambda}{2T_s}$$

where

$$V_{amb} = 2\omega|\sin\beta|r_t\,,$$

for rotational targets. The unambiguous velocity region in the range-Doppler image is defined by those velocities V which satisfy $|V| < V_{amb}/2$. Clearly, if we increase the interpulse spacing, then the unambiguous velocity region shrinks.

For example, consider a pulse train with an interpulse spacing of 1 μs and an optical wavelength of 10 μm, with a corresponding ambiguous range of 150 m and an ambiguous velocity of 5 m/s. Thus, within the range and Doppler window, the relative range and velocity of targets that are separated by less than 150 m in range and 5 m/s in velocity can be unambiguously measured. Equivalently, a waveform interpulse spacing of 1 μs provides an unambiguous velocity region of 1 MHz. As a result, targets with rotational Doppler spectra that are less than 1 MHz wide can be imaged without spectral foldover, or aliasing, in the Doppler dimension of the images.

Range-Doppler laser radars must make an effective trade-off between the range and Doppler ambiguities to match the target scenario. If the limitations that the waveform imposes on the unambiguous range and Doppler intervals become too prohibitive, then nonperiodic waveforms with no range or Doppler ambiguities must be used.

Waveform Performance Comparisons

The resolution and ambiguity response of a given waveform can be considered by analyzing its range-Doppler ambiguity function. The ambiguity function gives the point-target response in an AFL image; the central-lobe portion gives the point-target response of an unambiguous SAFL image.

Figure 10 shows three-dimensional surface plots of portions of the range-Doppler ambiguity functions for a 12-pulse train for each of the three waveform types. The plots in the left column of the figure show a view that includes the first range and Doppler ambiguity peaks for each waveform. The plots in the right column of the figure show a close-up view of the response about the mainlobe region for each waveform. The ambiguity function response was truncated at 20% of the mainlobe peak value to emphasize the structure of the sidelobe responses.

Each ambiguity function shown in Fig. 10 has a single-pulse TB product of 127 (pulse train TB product of 1524). The single-pulse TB product was chosen to be consistent with a moderate maximal-length sequence length of 127 for the periodic BPSK waveform. The BPSK and LFM chirp pulse trains are constant-envelope waveforms with $T_s = T_p$. To form a periodic sequence

Table 1. Waveform Performance Parameters

Waveform & (Parameters)	*Measurement*	*Performance Issues*		
		Resolution	*Ambiguity Peaks*	*Sidelobe to Mainlobe Ratio*
unmodulated pulse (T_p)	range Doppler	$cT_p/2$ $1/T_p$	none none	0 –13 dB
unmodulated pulse train (T_p, N_pT_s)	range Doppler	$cT_p/2$ $1/(N_pT_s)$	$cT_s/2$ $1/T_s$	0 –13 dB
LFM chirp pulse (T_p, B)	range Doppler	$c/2B$ $1/T_p$	none none	–13 dB –13 dB
LFM chirp pulse train (T_p, B, N_pT_s)	range Doppler	$c/2B$ $1/(N_pT_s)$	$cT_s/2$ $1/T_s$	–13 dB –13 dB
BPSK pulse* (T_p, τ_c, n_c)	range Doppler	$c\tau_c/2$ $1/T_p$	none none	$1/n_c$ –13 dB
BPSK pulse train (T_p, τ_c, n_c, N_pT_s)	range Doppler	$c\tau_c/2$ $1/(N_pT_s)$	$cT_s/2$ $1/T_s$ ($1/\sqrt{n_c}$ below mainlobe)	$1/n_c$ –13 dB

* The maximal-length sequence modulated single BPSK pulse is processed in a periodic manner to guarantee the low range sidelobes.

with low-range sidelobes, constant-envelope modulation of the BPSK waveforms is accomplished by repeating maximal length sequences. For comparison purposes, amplitude weighting was not applied in either the range or Doppler dimension.

The constant-envelope LFM and BPSK waveforms both have an advantage over the unmodulated pulse train waveform in terms of lower peak pulse-power requirements for a given range resolution. The BPSK waveform has better range resolution than the LFM waveform for a given TB product because amplitude weighting for range-sidelobe reduction is not required. For large single-pulse TB products, the BPSK range sidelobes are lower than the LFM sidelobes. Finally, the BPSK Doppler ambiguity peaks are well below the central ambiguity response peak. Hence the Doppler ambiguities are significantly reduced with the BPSK waveform. Table 1 summarizes the performance of the three unweighted single-pulse and pulse train waveforms.

Stretch Processing

The Firepond receiver is based on the *stretch* processing method. Stretch processing refers to the correlation mixing method used to process the LFM chirp pulse waveform. Instead of forming a digital or analog MF to the return wideband LFM chirp pulse signal $\mathbf{s}(t-\tau)$, we mix (multiply) a reference LFM chirp pulse signal $\mathbf{s}^*(t)$ with the return. The relative timing τ between the two

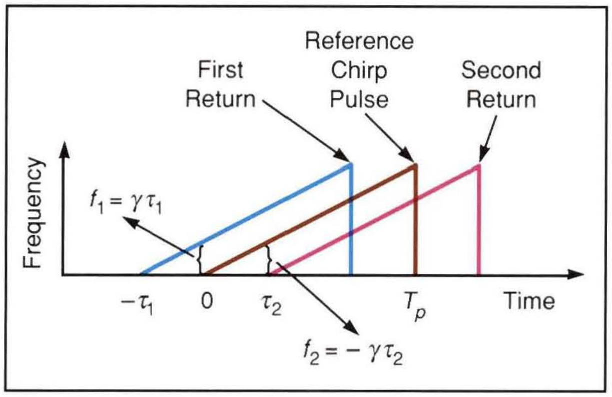

Fig. 11—Stretch correlation process with two point-target returns. The first return corresponds to an in-range target, and the second return corresponds to an out-range target.

chirp signals controls the maximum output frequency of the correlation mixer; the reduced-bandwidth output signal of the correlation mixer is then sampled and processed. Of course, limiting the maximum relative timing difference also limits the radar range window. Thus stretch processing provides a trade-off between processing bandwidth and range window.

Figure 11 illustrates the stretch correlation-mixing process for two point-target returns. If the point-target return arrives at time τ relative to the start time of the reference chirp train, then a difference frequency $\gamma\tau$, where γ is the chirp rate, is produced. Alternatively, the time-of-arrival difference $\tau = 2R/c$ produces a frequency difference $2\gamma R/c$ that corresponds to a target at relative range R. Thus the output frequency of the correlation mixer is proportional to the relative delay or range between the return and reference chirp pulse. This process is repeated for each corresponding pulse pair in the return and reference pulse trains.

The stretch receiver correlates the received signal envelope with respect to the reference signal envelope over a limited relative time-delay window, and then performs low-pass filtering. The low-pass filter (LPF) bandwidth is chosen to match the processing bandwidth of the A/D converter that follows the LPF. Correlation-mixer output signals that fall within the LPF bandwidth are passed without modification; any signals outside the band are integrated or removed by the LPF.

Stretch processing reduces the required processing bandwidth of a wideband signal by performing the correlation over a limited relative delay region, so that the corresponding correlation-mixer output signal spectrum passes through the LPF without modification. Thus, within the relative time-delay window, and therefore within the passband of the LPF, the stretch receiver response is equivalent to the correlation or MF receiver response.

The LFM chirp pulse train and the stretch processor are particularly well suited to produce SAFL images. The first step of the SAFL imaging process is to form a single-pulse MF to the return pulse train. With the stretch processor, single-pulse correlations are formed, and these correlation outputs are Fourier transformed to form the equivalent single-pulse MF output. The correlation-mixer output for a point-target return $\mathbf{s}(t)$ at a relative range $c\tau_0/2$ and Doppler frequency shift ϕ_0 with respect to the kth reference pulse is

$$\mathbf{y}_k(t;\tau_0,\phi_0) = \mathbf{s}(t-\tau_0)e^{j2\pi\phi_0 t}\mathbf{p}^*(t-kT_s)$$

where the stretch receiver tightly controls the relative timing delay $\tau_0 < T_s$. The Fourier transform of this difference signal gives the kth single-pulse MF output

$$\begin{aligned} Y_k(f;t_0,\phi_0) &= \int_{-\infty}^{\infty} \mathbf{y}_k(t;\tau_0,\phi_0)e^{-j2\pi ft}dt \\ &= \int_{-\infty}^{\infty} \mathbf{s}(t-\tau_0)\mathbf{p}^*(t-kT_s)e^{-j2\pi(f-\phi_0)t}dt. \end{aligned} \tag{12}$$

When $\mathbf{s}(t)$ is an LFM chirp pulse train and $\mathbf{p}(t)$ is an LFM chirp pulse, then the relationship between the single-pulse MF response (Eq. 10) and the Fourier-transformed difference signals (Eq. 12), to within a constant phase term, is

$$\mathbf{y}(kT_s - iT;\tau_0,\phi_0) = Y_k(i\gamma T;\tau_0,\phi_0), \tag{13}$$

over the relative timing-delay region, where $i\gamma T$ is within the stretch processor bandwidth. The stretch-processed SAFL image is given by Eq. 10, with the substitution defined by Eq. 13. In retrospect, the SAFL image formation with a stretch processor amounts to performing a two-dimensional DFT on the correlation-mixer output signal, where the single-pulse correla-

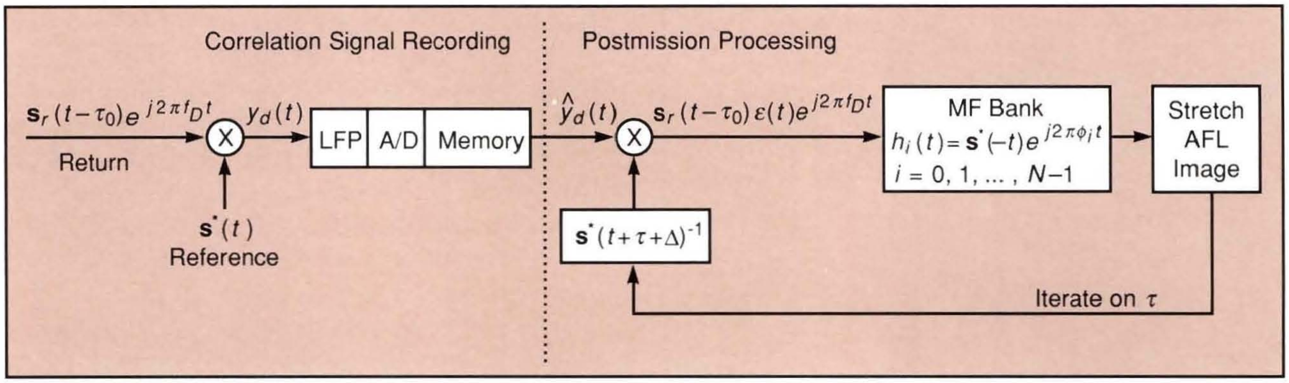

Fig. 12—Recovery of the return signal envelope $\mathbf{s}_r(t)$ *from the correlation-mixer output. The difference signal from the correlation-mixer output is sampled and stored; the target return envelope is then recovered via the postmission iteration process.*

tion-mixer output signals are arranged to form the rows of the input data set. Zero padding for increased image resolution and amplitude weighting of the input data set for reduced sidelobes is readily accomplished in the two-dimensional DFT format.

Range-Doppler Coupling of the LFM Chirp Pulse Response

The ambiguity-function response of an LFM chirp pulse causes a coupling of the range and Doppler errors. In other words, an error in the timing of the return pulse (target range) results in the same MF response that would be obtained with a corresponding error in the estimate of the carrier frequency of the return waveform (target velocity).

With stretch processing of the LFM pulse, a time delay is equivalent to a frequency shift of the output correlation signal. Hence an LFM chirp pulse train cannot be used simultaneously to form an image and to provide for unambiguous tracking of the target range and radial velocity (Doppler). This coupling phenomenon does not degrade the stretch-processed SAFL image; however, the SAFL image may lie on an ambiguity peak. Radial target velocity information can be obtained by transmitting an unmodulated constant-frequency pulse that is processed to provide Doppler and low-range resolution data. Another way to resolve the coupling in range and Doppler is to sweep the LFM up and down on alternate pulses to remove

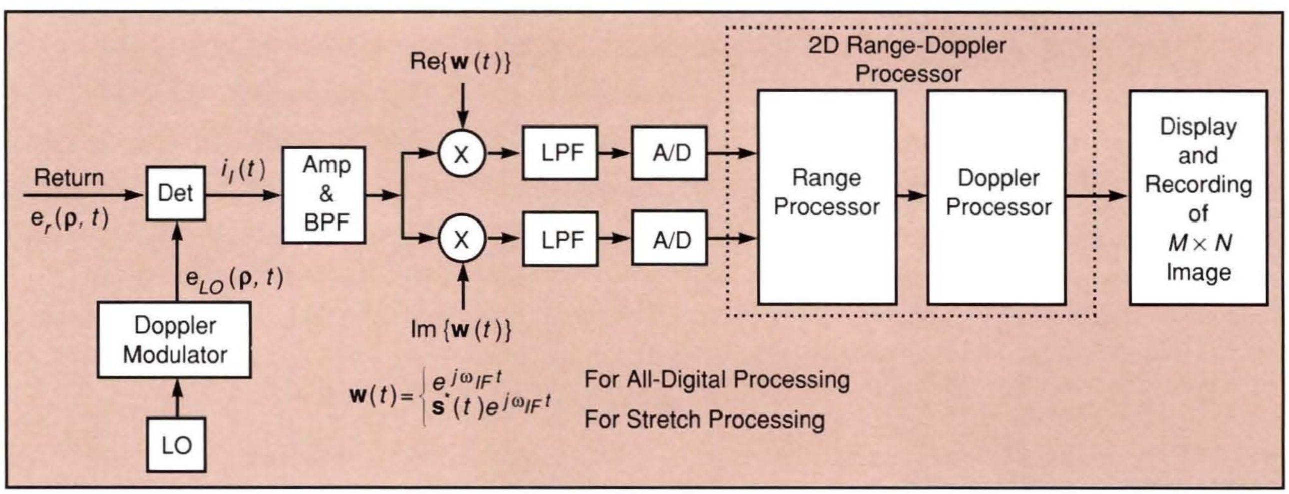

Fig. 13—Heterodyne receiver and generic waveform processor. The correlation reference signal $\mathbf{w}(t)$ *is an IF tone for the all-digital processor and a linear frequency-modulated (LFM) chirp pulse train for the stretch processor.*

the ambiguity. Various combinations of unmodulated pulse and/or LFM up-down waveforms allow for simultaneous imaging and tracking.

AFL Image Formation with a Stretch Processor

The Firepond system is based on the generation and stretch processing of chirp waveforms. Nonperiodic but coherent chirp waveforms can be used to create AFL images with a stretch processor. Such waveforms might be composed of a single LFM or nonlinear FM chirp pulse, an up-down chirp pulse pair, or chirp pulse trains composed of combinations of up-down LFM chirps of varying bandwidths and interpulse spacings. AFL images that are range-windowed versions of the ambiguity function can be formed with a stretch receiver. A direct but hardware-intensive method is to use a bank of correlation mixers. Each mixer is offset in frequency by an amount corresponding to the desired Doppler frequency resolution of the image.

A software-generated AFL image can be produced provided that the received signal envelope is recorded. The received signal envelope can be recovered, over a relative range window with a single complex correlation-mixing stage, provided that the relative timing between the return signal and the correlation reference signal is known precisely. Given the relative timing, the inverse, or conjugate, phase of the correlation signal can be applied to the recorded difference signal to yield the complex signal envelope. Figure 12 illustrates the process of recovering the complex envelope of the return signal.

The captured return-signal envelope $\hat{\mathbf{s}}_r(t)$ from the stretch receiver is of the form

$$\hat{\mathbf{s}}_r(t) = \mathbf{s}_r(t - \tau_o)\varepsilon(t)e^{j2\pi f_D t}$$

where f_D and τ_o are the unknown relative Doppler shift and timing difference between the return signal envelope $\mathbf{s}_r(t)$ and the reference signal envelope $\mathbf{s}(t)$, respectively. The error in removing the correlation signal is given by

$$\varepsilon(t) = \frac{\mathbf{s}^*(t)}{\mathbf{s}^*(t+\Delta)}$$

where Δ is the relative timing error between the correlation signal and the inverse correlation signal. In the ideal condition, the relative timing error Δ equals zero, which forces the multiplicative phase error $\varepsilon(t)$ to unity. An iterative process of shifting the inverse correlation signal can be used to estimate when $\Delta = 0$; this process may be computationally intensive for waveforms with high TB products. The amount of relative timing precision required to produce good AFL images depends on the waveform as well as the amount of stretch processing, if any.

Waveform Processors

Figure 13 shows a simplified block diagram of a generic receiver and waveform processor. The mixer reference signal is either an LFM chirp pulse train phase-modulated IF carrier for stretch processing or an unmodulated IF carrier for all-digital processing (an alternate form of the receiver allows correlation to be done optically with the LO signal). The processor relies on an A/D sampling rate and LPF filter bandwidth consistent with the desired difference signal bandwidth. The receiver samples the entire return pulse train waveform, with a sufficiently large A/D start-time and stop-time window (sampling window) to guarantee capture of the complete train waveform, then performs digital matched filtering and processing. For stretch processing, the start time of the reference chirp pulse train (based on the predicted target range from the tracking filter of the radar) determines the center of the target range window.

The all-digital processor has an advantage in hardware simplicity, although the critical piece of hardware is the high-speed A/D converter. The sampling window position can be crudely estimated to guarantee capture of the return waveform, but the absolute range accuracy depends on knowing the precise A/D start time. Well-developed real-time array-processing technology makes the digital matched filtering method attractive.

The stretch processor has the advantage that the chirp pulse bandwidth can be fully utilized to provide very fine range resolution, while the required receiver sampling rate (receiver band-

Table 2. Waveform Processing Steps for SAFL Images

Step	*All Digital*	*Stretch*
1	Initialization steps	
	Store the complex conjugate of the DFT of the zero-padded and amplitude-weighted single pulse reference; the DFT size must match the expected number of samples over the A/D sampling window. Store the Doppler amplitude weights.	Store the range and Doppler amplitude weights.
2	Transmit the pulse train waveform and sample the return signal.	
	Position the A/D window around the crudely estimated time of arrival (TOA) of the return. Record the precise time of the first sample.	Generate the correlation reference signal precisely at the estimated TOA of the return; sample the difference signal over the crudely positioned A/D window.
3	Compute the single-pulse MF response and realign the samples in time (modulo the interpulse spacing).	
	Compute the DFT of the complete sampled return; this DFT output is multiplied by the stored complex-conjugate single-pulse spectrum. Compute the inverse DFT of the product spectrum; this is the single-pulse MF output. Align the periodic MF output on a pulse-by-pulse basis.	Apply range weighting and compute the zero-padded DFT of each pulse's weighted mixer output; these make up the single-pulse MF response. Align the DFT outputs on a pulse-by-pulse basis.
4	Apply zero padding and amplitude weighting to the nonzero Doppler samples along each fixed relative range bin. Compute the DFT of these Doppler samples at each range bin; this is the image response at each range bin. Display the squared magnitude of the resultant image.	

width) is much lower than the normal Nyquist sampling rate required for the chirp pulse bandwidth. However, the penalty in this processing method is that the range window of the radar is a fraction of the potential unambiguous range window allowed by the chirp train waveform.

The Firepond system utilizes I- and Q-channel A/D converters, each of which can sample at a 200-MHz rate with 8 bits of resolution and store up to 128K samples. Thus Firepond has the capability to process very high-resolution waveforms with the stretch processing method. Tables 2 and 3 describe the major waveform processing steps to produce SAFL and AFL images with zero padding and amplitude weighting. Table 2 describes how SAFL imaging with a stretch processor is accomplished by a series of one-dimensional DFT operations: the input data set can also be arranged in a two-dimensional format, with amplitude weighting and zero padding, and then transformed to form the image in a single two-dimensional DFT operation.

Image Enhancement

In general, many image-enhancement or feature-extraction techniques are available for applications such as automatic target recognition. The image-enhancement techniques considered here are amplitude weighting for increased dynamic range between pixels, zero padding for increased image resolution, and incoherent averaging for increased image SNR.

Range-Doppler stretch-processed data were collected at the Firepond indoor test range by using a conically shaped and spinning test target at spin-axis orientations of 14.5°, 45°, and 90°, with respect to the radar viewing angle. The cone spin rate was 2 rev/s at the 14.5° viewing angle, and 1 rev/s at the 45° and 90° viewing angles. The range-Doppler waveform was a 25-pulse LFM chirp pulse train. The target return waveform was stretch processed with 32 samples (range) taken of the correlation, or difference, signal across each of the 25 pulses. Thus the fundamental range-Doppler image dimensions are 32 range pixels by 25 Doppler, or cross-range, pixels. The following sections show images constructed from this data set to illustrate these processing techniques.

Zero Padding

When the matched filters used in either the SAFL or AFL image process are implemented in the DFT domain, the DFT output resolution can be improved by adding zeros to the input data

Table 3. Waveform Processing Steps for AFL Images

All Digital	*Stretch*
1 Initialization steps	
Store the *N* reference spectra, one for each Doppler bin. Each spectrum is the DFT of the zero-padded and amplitude-weighted reference waveform at a particular Doppler frequency; the DFT size must match the expected number of samples over the A/D sampling window.	
2 Transmit the pulse train waveform. Sample and record the return signal over the A/D window.	
Position the A/D window around the crudely estimated time of arrival (TOA) of the return. Record the precise time of the first sample.	Generate the correlation reference signal precisely at the estimated TOA of the return; sample and record the difference signal over the crudely positioned A/D window. Reconstruct the return signal envelope via an iteration process that removes the correlation-mixer reference signal.
3 Compute the DFT of the complete sampled return. Multiply this DFT output spectrum by the complex-conjugate reference spectrum corresponding to a particular Doppler bin. Compute the inverse DFT of the product spectrum; this is the image response at that Doppler bin. Repeat for all other Doppler bins and display the squared magnitude of the resultant image.	

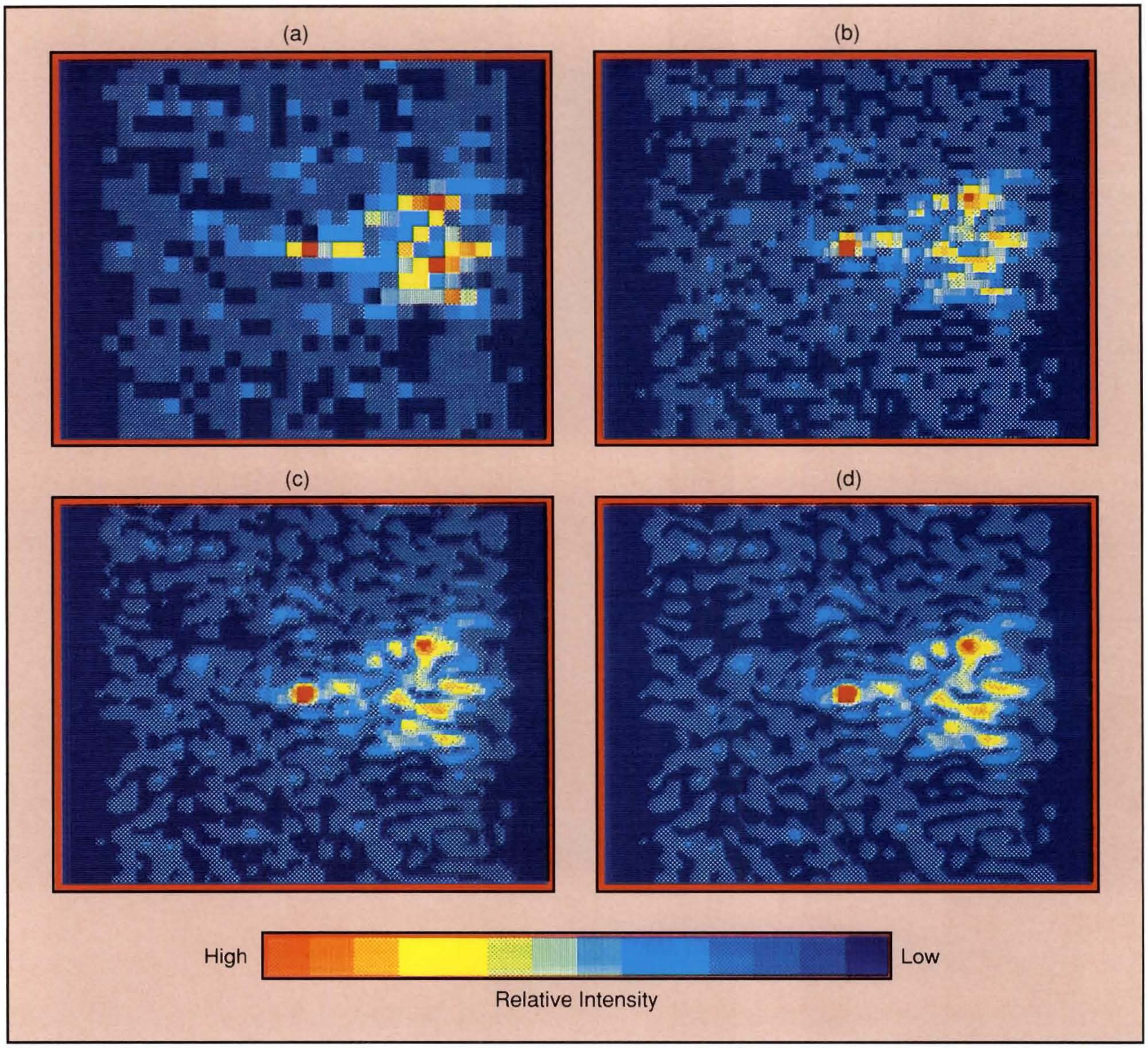

Fig. 14—Zero-padded range-Doppler images of a spinning cone: (a) no zero padding (32 × 25 pixels), (b) 50% zero padding (64 × 50 pixels), (c) 75% zero padding (128 × 100 pixels), and (d) 87.5% zero padding (256 × 200 pixels).

set. Figure 14 shows four versions of a single image of the spinning cone for the 14.5° viewing angle. The four versions include the same image produced with no zero padding and with 50%, 75%, and 87.5% zero padding, respectively, of the input data set in each dimension. The percentage padding is defined as $100n_z/(n_p+n_z)$, where n_z is the number of zeros and n_p is the number of nonzero samples. The highest-intensity pixels in the center of the image, which correspond to the zero-range zero-Doppler position, are due to a DC bias voltage in the correlation mixer output. For purposes of display, the images are linearly scaled with respect to the highest-intensity target pixel; the pixels in the zero-range zero-Doppler region are truncated to the level of the highest-intensity target pixel. Clearly, even though zero padding does not change the waveform resolution, it improves the output resolution of the image. Zero padding, which brings out features that would not be visible otherwise, allows the output image resolution to match or better the resolution of the image media.

Amplitude Weighting and Incoherent Averaging

Amplitude weighting of the receiver's MF may be necessary to reduce the range and Doppler sidelobes at the expense of a broadened mainlobe response. A Hamming-weighted window has a 3-dB mainlobe beamwidth approximately 46% larger than the beamwidth of a uniform window [10]. The loss in processing gain with Hamming weighting as compared to uniform weighting is about 1.34 dB; this loss becomes 2.68 dB when Hamming weighting is applied to both of the image dimensions. Figure 15 compares the relative sidelobe levels for uniformly weighted or Hamming-weighted windows of width *W*.

Figure 16 shows the effects of Hamming weighting on image quality in a series of images with 75% zero padding, both with and without two-dimensional Hamming weighting, for each radar viewing angle. Images produced from the incoherent average of 25 consecutive single-frame images are also shown. Incoherent averaging reduces speckle and shot-noise variations while intensifying the target pixels. The figure clearly illustrates that zero padding and incoherent averaging improve the quality of the image.

Figure 16 also shows the spatially averaged CNR and image SNR for each image, where a spatial object mask, or outline, was defined for each viewing angle. The average CNR is highest at the 45° viewing angle and lowest at the 14.5° viewing angle. The target pixels near the base of the cone and central-Doppler region have the highest CNR values (20 to 28 dB); the target pixels near the cone tip and high-Doppler edges have much lower CNRs. The single-frame image SNR varies considerably from frame to frame partly because of the relatively small number of target pixels used in the spatial average. The average image-SNR improvement with 25-frame incoherent averaging is approximately 11 dB for the unweighted images and 10 dB for the Hamming-weighted images; the ideal SNR improvement is 14 dB. Hamming weighting enhances the high-CNR pixels, while some of the single-frame image features are lost for low-CNR pixels, due to the 2.68-dB loss in processing gain. Hamming weighting, in combination with a fixed object mask, artificially improves the average CNR and image SNR by broadening the response of each object pixel.

Figure 17 shows an image with 75% zero padding of a target complex that consists of a rigid four-ball constellation on a rotating platform. The image shows that the near-range (bottom) balls and far-range (top) balls are moving at a radial direction perpendicular to the radar line of sight. Thus their Doppler signatures are much smaller than the two midrange balls whose velocity components are greater from the radar's viewing angle. In the four-ball image, the average CNR is 29.3 dB with no weighting and 27.9 dB with Hamming weighting; the average CNR is defined as the average of the peak CNR from each ball.

Figure 18 compares a single-frame SAFL image of the spinning cone at a 14.5° viewing angle to a reconstructed AFL image, by using the same set of stretch-processed I- and Q-channel difference signal data. Because the periodic LFM chirp waveform was used, a relative timing error in the reconstruction process simply results in range shift of the image. As expected, the stretch-processed AFL and

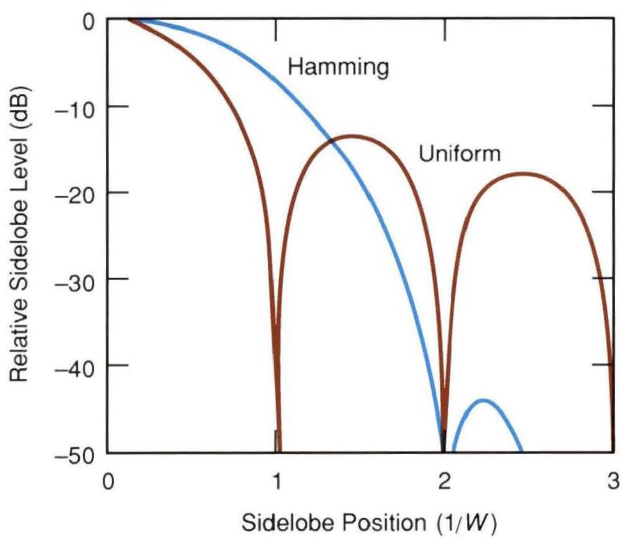

Fig. 15—Comparison of relative sidelobe levels for uniformly weighted and Hamming-weighted windows of width W.

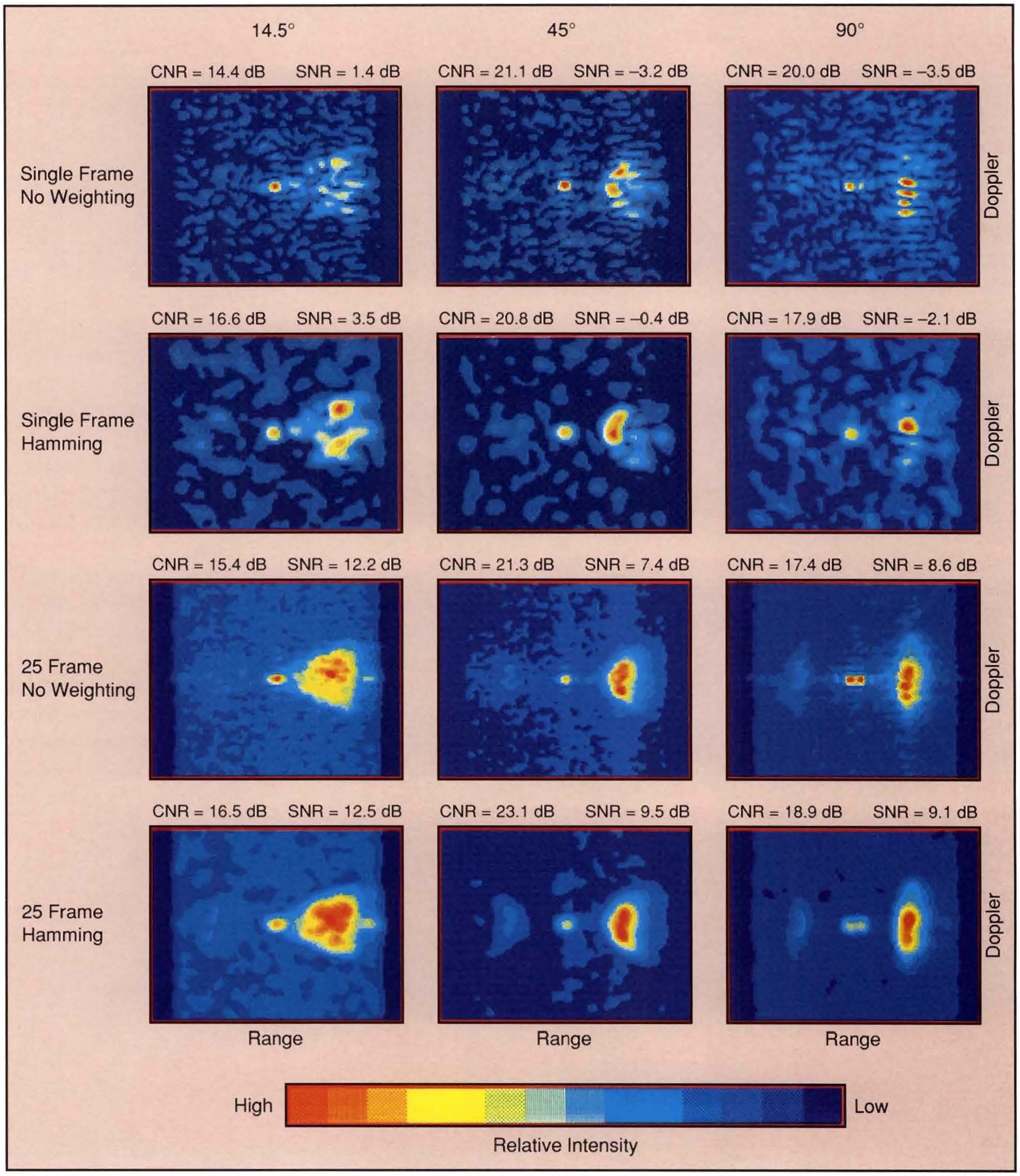

Fig. 16—Unweighted, Hamming-weighted, and 25-frame incoherent-averaged zero-padded images of a spinning cone at three viewing angles.

SAFL images are nearly identical.

Errors and Error Models

The primary error sources can be characterized in terms of their effect on the received waveform envelope. Let us define a generic nonideal point-target return-pulse-train complex-waveform envelope $\mathbf{s}_{\varepsilon}(t)$ in the following manner:

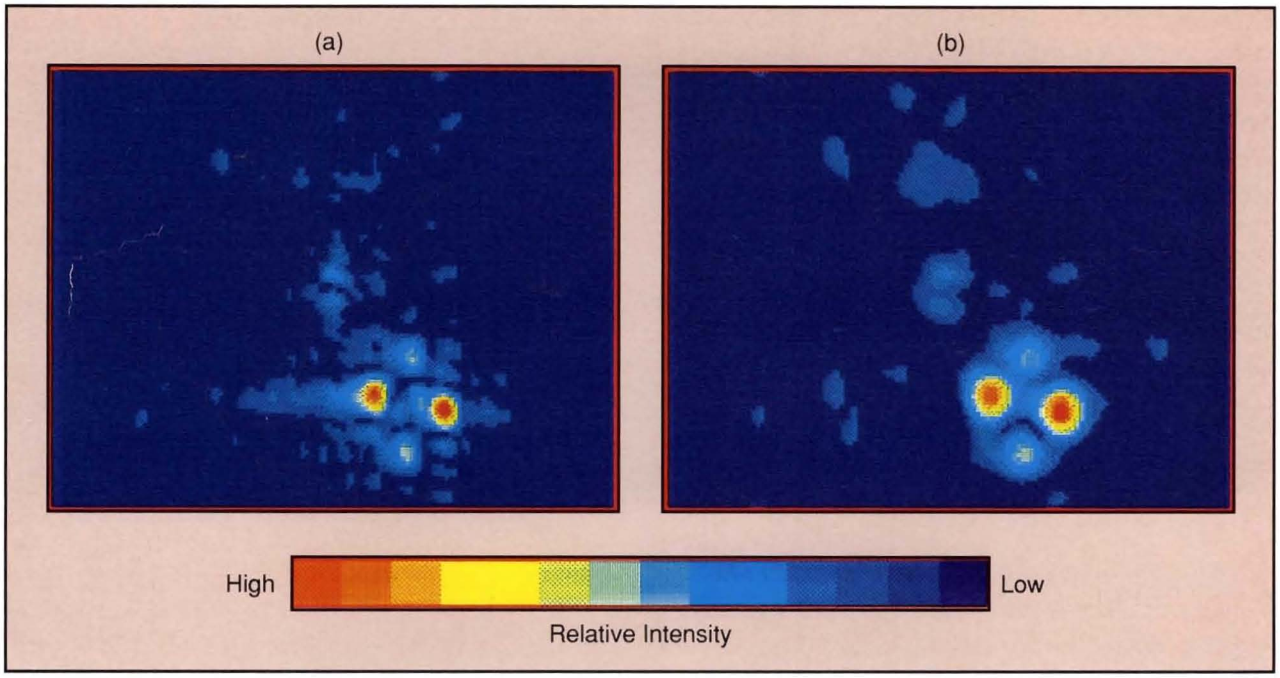

Fig. 17—Single-frame 75% zero-padded (128 × 100 pixels) images of a rigid four-ball constellation on a rotating platform: (a) no amplitude weighting, (b) Hamming weighting in range and Doppler.

$$\mathbf{s}_\varepsilon(t) = \varepsilon(t) \sum_{k=0}^{N_p - 1} \mathbf{p}(t - kT_s + \alpha_k) \qquad (14)$$

where the individual pulse envelopes are characterized by the ideal complex envelope $\mathbf{p}(t)$, and the complex envelope of the error is

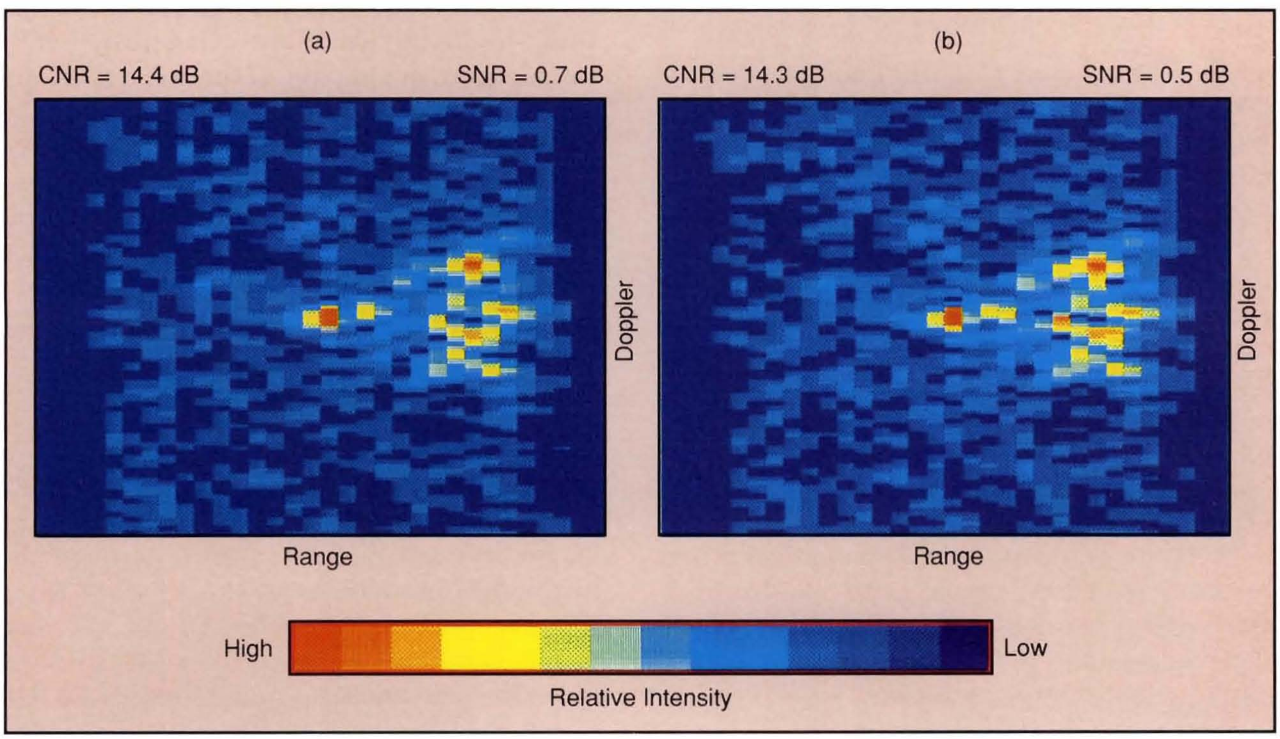

Fig. 18—(a) SAFL image and (b) stretch-processed AFL image of a spinning cone. Each image is 32 × 100 pixels.

given by $\varepsilon(t)$. The timing error, or jitter, associated with the kth pulse is α_k. Equation 14 gives the ideal transmitted waveform envelope with $\varepsilon(t) = 1$ and $\alpha_k = 0$. The pulse-to-pulse timing errors $\{\alpha_k;\ k = 0, 1, \ldots, N_p\}$ can be modeled as random variables drawn from either a zero-mean uniform distribution or a zero-mean Gaussian distribution.

The complex error function $\varepsilon(t)$ models the amplitude and phase errors introduced into the transmitted waveform envelope. The errors are usually of the following six types.

Cubic phase, or quadratic frequency, errors. The form is

$$\varepsilon(t) = e^{j2\pi\gamma_e t^3/3}$$

where γ_e is the rate of the quadratic frequency variation. This type of phase error occurs because of refractive index changes in the laser gas medium, which are caused by thermal heating of the gas during discharge. The changes in refractive index result in variation of the optical path length, and thus variation in the phase of the transmitted waveform.

Quadratic phase, or LFM chirp, errors. The form is

$$\varepsilon(t) = e^{j\pi\gamma_e t^2}$$

where γ_e is the rate of the linear frequency variation. This type of phase error models such phenomena as linear drift in the MO frequency relative to the LO frequency in the receiver, optical path-length variation through the wideband laser amplifier, or voltage drooping of the traveling wave tube (TWT) power supply that drives the wideband electro-optic modulator and results in a linearly increasing delay across the waveform envelope.

Linear phase errors. The form is

$$\varepsilon(t) = e^{j2\pi(\Delta f)t}$$

where Δf represents a difference frequency error between the transmitter and receiver reference oscillators. The difference error results from an error in the radar receiver's estimate of the relative Doppler shift between the transmitted and the return waveform (due to translational target motion along the radar's line of sight), or from receiver frequency biases that may occur in sources such as the IF mixing stages.

Random phase errors. The form is

$$\varepsilon(t) = e^{j\Theta(t)}$$

where $\{\Theta(t_i), \Theta(t_j)\}$ are independent random variables for $i \neq j$. The variables $\{\Theta(t_i)\}$ are assumed to be either zero-mean Gaussian or uniform random variables with a specified standard deviation σ_θ. The phase-error spectral bandwidth is assumed to be much greater than the complex-envelope bandwidth of the particular waveform of interest.

Sinusoidal phase errors. The form is

$$\varepsilon(t) = e^{jA_\theta \sin(\omega_0 t + \Phi)}$$

where A_θ is the peak phase-error amplitude, ω_0 is the radian frequency of the phase error, and Φ represents the uniformly distributed (over 2π) random starting phase of the sinusoidal error. This type of error models potential phase-error ripples that occur in the passbands of the signal generation and filtering electronics.

Amplitude errors. The form is

$$\varepsilon(t) = a(t)$$

where $a(t)$ is a deterministic or random amplitude-distorting function. Generally, some rounding off, or shaping, of the pulse envelopes occurs because of bandwidth limitations or passband roll-off of the transmitter electronics, and passband filtering sometimes generates a sinusoidal amplitude ripple. Additional amplitude variations are caused by the nonuniform gain of the wideband electro-optic modulator and of the wideband laser amplifier.

Performance Measure

The system performance requirements are determined by simulating the effects of the various error types on the processed return waveforms. Although several performance measures can be considered, including loss of processing gain and resolution [10], the most significant (and the most sensitive to small errors) is the sidelobe-to-mainlobe ratio (SLMR), which is a measure of the system dynamic range. The system dynamic range determines

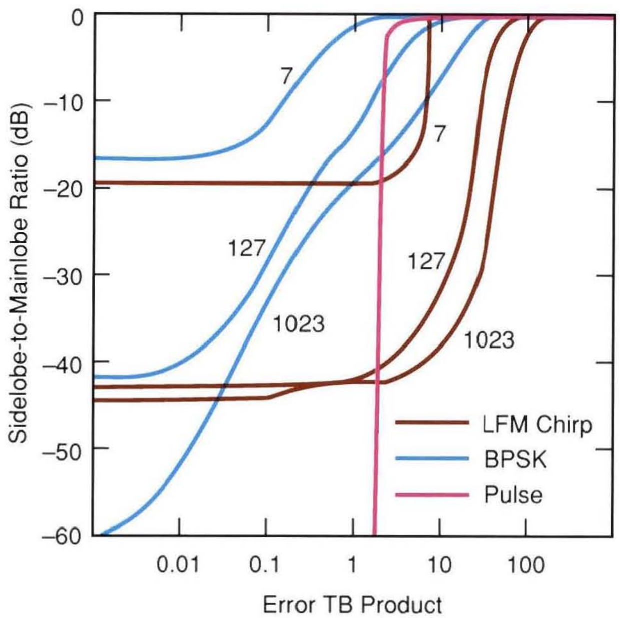

Fig. 19—Sidelobe-to-mainlobe ratio performance of the three waveforms for three single-pulse TB products, in the presence of a quadratic phase error. The unmodulated pulse performance does not depend on its TB product.

the ability to detect a small-target signal return in a given range or Doppler bin when a much larger signal is present in some nearby bin. A sidelobe is, by definition, a local maximum in the MF response that is below the mainlobe response peak. Because more than one local maximum generally occurs, the SLMR is specified by using the maximum sidelobe value. The sidelobe fall-off rate, which is also sometimes used as a performance measure, is not considered here.

Range and Doppler Sidelobes

We first consider the range processing of the coherent pulse train. If Hamming or other pulse amplitude weighting is applied in the receiver processing to reduce the range sidelobes, then the single-pulse MF impulse response is of the form

$$\mathbf{h}(t) = \mathbf{p}^*(-t)w_p(-t)$$

where $w_p(t)$ is the amplitude-weighting function. If Hamming weighting is applied, then $w_p(t)$ is the standard raised-cosine weighting function.

We define the amplitude-weighted single-pulse cross-correlation function in the presence of a generalized error function to be

$$R_{p\varepsilon}(k,\tau) = \int_{-\infty}^{\infty} \varepsilon(\lambda)\mathbf{p}(\lambda - kT_s + \alpha_k)\cdot \mathbf{p}^*(\lambda-\tau)w_p(\lambda-\tau)d\lambda .$$

By definition $R_{p\varepsilon}(k, \tau)$ is zero outside the interval $[kT_s - T_p \le \tau \le kT_s + T_p]$. The complex envelope of the single-pulse MF output for a zero-range, zero-Doppler point-target return $\mathbf{s}_\varepsilon(t)$ from Eq. 9 is

$$\mathbf{y}(t) = \sum_{k=0}^{N_p - 1} R_{p\varepsilon}(k,t). \tag{15}$$

For single-pulse, range-sidelobe performance we look at the behavior of $R_{p\varepsilon}(k, \tau)$. Depending on the error function and the coherent waveform type, some variation occurs in the single-pulse performance as a function of the pulse position in the train waveform.

The periodic single-pulse sidelobe performance of the kth pulse in the constant-envelope waveform train is determined by the behavior of

$$R_{p\varepsilon}(k-1,\tau) + R_{p\varepsilon}(k,\tau) + R_{p\varepsilon}(k+1,\tau), \quad \text{for } kT_s - T_p \le \tau \le kT_s + T_p .$$

Essentially, the single-pulse MF sidelobe response depends on the contribution from an adjacent pulse.

Figure 19 compares the range SLMRs of each of the three primary pulse types (simple unmodulated pulse, LFM chirp pulse, and BPSK pulse) for three single-pulse TB products (TB = 7, 127, 1023) in the presence of a quadratic phase error. In the figure, the SLMR is plotted versus the error TB product, which is $\gamma_e T_p^2$ for the quadratic phase error. The phase errors are assumed to extend over the three-pulse intervals when the single BPSK pulse is processed periodically (i.e., match filtered to a three-pulse waveform).

The performance curves show that the BPSK pulses (processed periodically) are clearly more sensitive to quadratic phase errors than are the Hamming-weighted LFM chirp pulses. Generally speaking, the sidelobe performance is dramatically reduced as the error TB product approaches the TB product of the complex

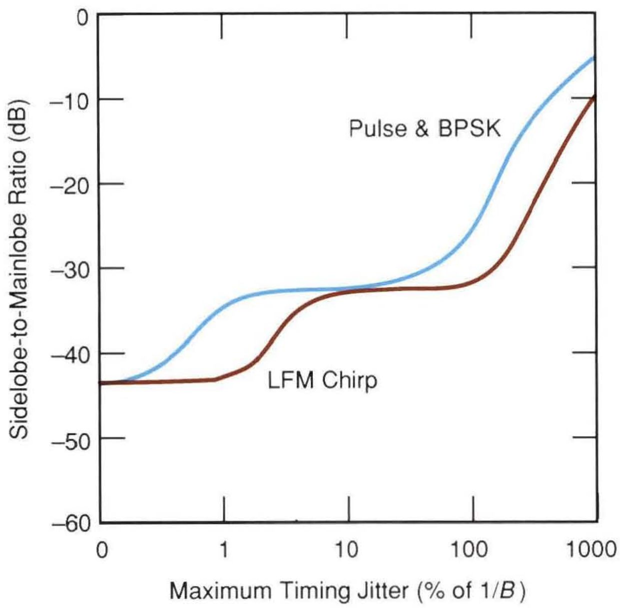

Fig. 20—Hamming-weighted Doppler-sidelobe performance in the presence of pulse-to-pulse timing jitter for a 128-pulse train.

waveform envelope. The performance of the simple unmodulated pulse is nearly binary; i.e., the ideal triangular shape of the autocorrelation function is distorted but with no sidelobes (or local maxima) until the phase deviation is approximately π radians across the pulse. At this point, multiple peaks are introduced into the mainlobe response.

Doppler processing for SAFL images is achieved by sampling and amplitude-weighting the single-pulse MF output given by Eq. 15. The Doppler response at the ith range bin of the SAFL image is

$$\left|\sum_{k=0}^{N_p-1} R_{p\varepsilon}(k, kT_s + iT + \alpha_k) w_D(k) e^{-j2\pi kn/N}\right|^2$$

$$\text{for } n = 0, 1, \ldots, N-1$$

where $w_D(k)$ is a discrete-valued N_p-point amplitude-weighting function, and each point corresponds to a pulse in the train.

Figure 20 compares the Doppler-sidelobe performance of the three primary waveform types in the presence of only pulse-to-pulse timing jitter α_k. The pulse-to-pulse behavior of the autocorrelation function $R_{p1}(k, \alpha_k)$, where $\varepsilon(t) = 1$, determines the Doppler-sidelobe level. Hamming amplitude weighting is performed on the individual LFM chirp pulses for range weighting, and Hamming weighting is applied across the train envelopes (consisting of 128 pulses) of all types of waveforms for Doppler-sidelobe weighting. The random timing errors α_k are assumed to be uniformly distributed on the interval $[-f/2, f/2]$, where f is a percentage of the waveform resolution $1/B$, and where B is the single-pulse bandwidth. Because the mainlobe response of the single-pulse autocorrelation function is triangular for both the BPSK and the simple pulse waveform, their average Doppler SLMR performance is nearly identical. The weighted LFM chirp pulse response is more tolerant of timing jitter errors, but primarily because the mainlobe response peak is broadened by the Hamming weighting.

If there is no timing jitter and the pulse-to-pulse Doppler sampling period does not vary, then the samples of the autocorrelation function $R_{p\varepsilon}(k, kT_s + iT)$ are constant across the Doppler measurement. In this case, the autocorrelation

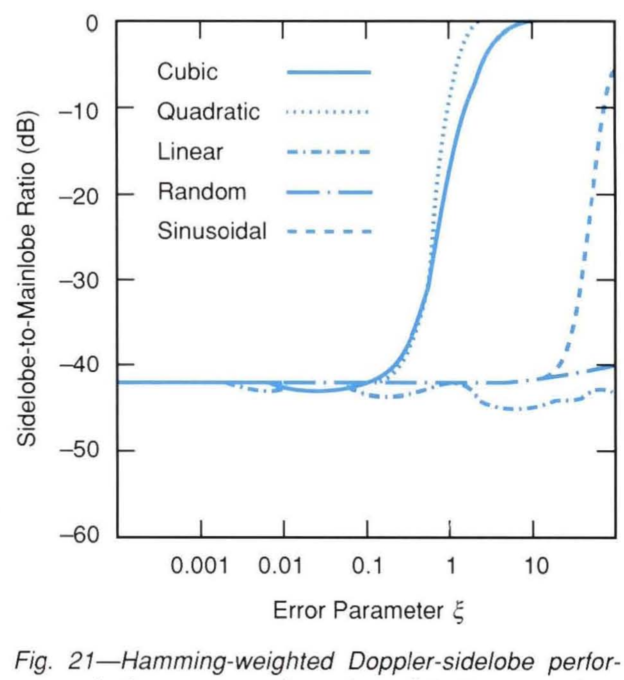

Fig. 21—Hamming-weighted Doppler-sidelobe performance in the presence of envelope distortion errors for a 32-pulse train. For the linear, quadratic, and cubic phase errors the error parameter ξ equals $\Delta f(N_p T_s)$, $\gamma_e(N_p T_s)^2$, and $\gamma_e(N_p T_s)^3$, respectively. For the random and sinusoidal phase errors the error parameter ξ equals σ_θ, and A_θ, respectively, both in degrees with $\omega_0 T_p/2\pi = 10$.

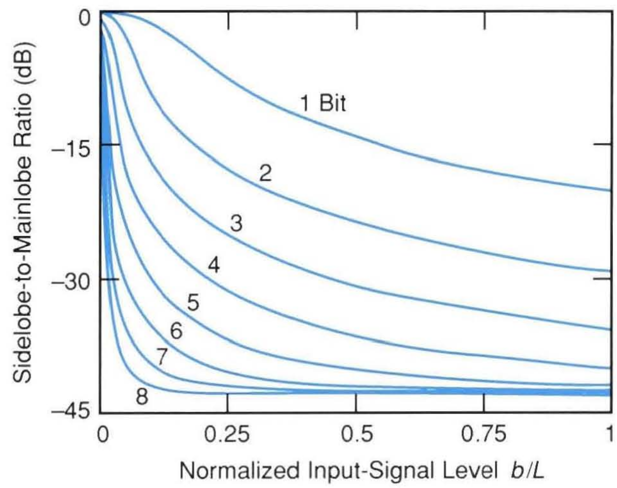

Fig. 22—Average SLMR for a constant input signal with Hamming weighting over the sampling window of 128 points as a function of the normalized input signal level. The number of A/D bits is varied from 1 to 8.

function is just the integral of the weighted or unweighted error function $\varepsilon(t)$. The variation of this time-averaged error function across the waveform measurement time determines the SLMR performance. Figure 21 shows the Doppler SLMR performance for each type of phase error as a function of its error parameter ξ. Additional details and performance curves can be found in Ref. 2.

A/D Quantization Error

Let us consider the simple case in which only quantization errors occur. If the input signal is a constant value b, then the kth output sample of the A/D converter is given by

$$s_k = b + \Delta u$$

where Δu is a uniformly distributed random variable. If the amplitude range of the input signals is [0, L], then an n-bit A/D has a least-significant bit, or quantization cell size, given by

$$a = \frac{L}{2^n - 1}.$$

In this notation, the random variable Δu is uniformly distributed over the interval $[-a/2, a/2]$ with zero mean and variance $a^2/12$. The SNR of the A/D output becomes

$$\mathrm{SNR} = \frac{b^2}{\sigma^2_{\Delta u}} = \frac{12b^2\left(2^n - 1\right)^2}{L^2}$$

where only quantization noise is considered.

Figure 22 shows the average range SLMR for a constant input signal with Hamming weighting, as a function of the normalized input signal level b/L for one through eight bits of quantization. The ideal condition $b = L$ occurs in automatic gain control systems in which the input signal level is matched to the dynamic range of the A/D converter. Approximately five bits are required to reach the sidelobe level of −42 db.

DFT Sample Set Size

The best SLMR that can be obtained with a given amplitude-weighted window (or data set) is a function of the number of nonzero sample points across the window or in the DFT input. Figure 23 shows that the Hamming sidelobe level is −40 dB down after 20 samples. The sidelobe level is considerably worse for a small odd number of samples than for an even number of samples, since an odd number induces an asymmetry in the Hamming weighting. Thus we prefer to use an even number of samples, at least until the number of samples is greater than 50.

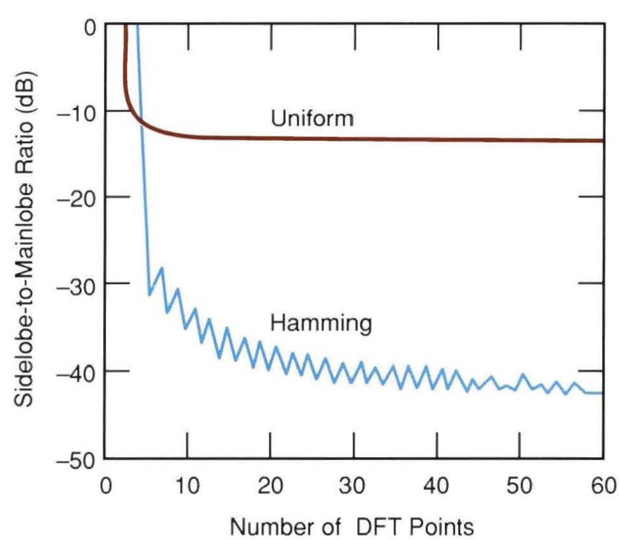

Fig. 23—SLMR as a function of the number of nonzero samples in the DFT. A uniform window is compared to a Hamming window.

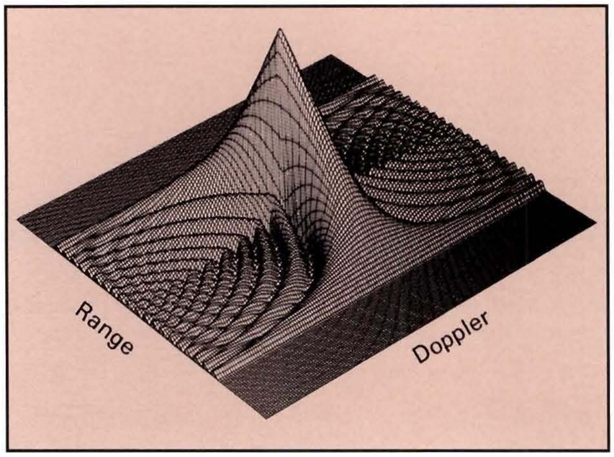

Fig. 24—Ideal single-unmodulated-pulse response.

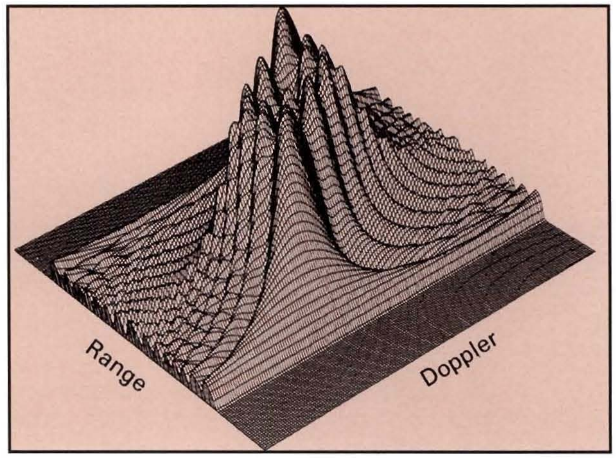

Fig. 25—Single-pulse matched-filter (MF) response with a quadratic phase error and without error compensation.

Amplitude and Phase Error-Compensation Scheme

The error-compensation scheme is used to reflect a small fraction of the transmitted optical signal to the receiver via the error-compensation signal path. Thus, while the laser radar waveform is in transit, the receiver samples the complex envelope of a replica of the transmitted waveform. This procedure assumes that the laser radar PRF is low enough to avoid conflicts from returning adjacent waveforms, and that the coherent waveform envelope duration is short compared to the round-trip travel time to the target. For systematic or recurring errors, the compensation process need not be performed on each transmitted waveform. This process can be employed as an error calibration procedure before mission operations.

For the all-digital receiver, the compensation process samples and stores the corrupted transmit waveform envelope $\mathbf{s}_\varepsilon(t)$; the receiver then forms an MF to this corrupted complex envelope. Systematic receiver errors contribute to the final form of the corrupted envelope. For the stretch-processor and constant-envelope LFM chirp waveforms, the difference signal for a point-target return is given by

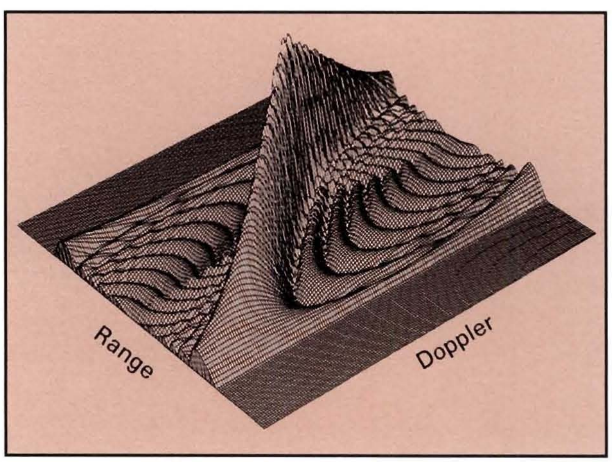

Fig. 26—Single-pulse MF response with a quadratic phase error and with ideal error compensation.

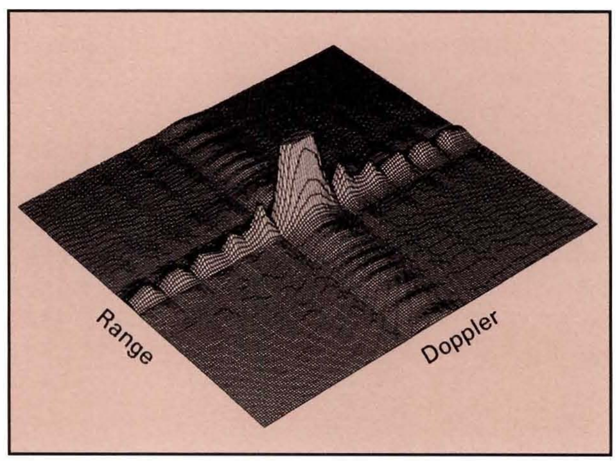

Fig. 27—Ideal ambiguity-function central-lobe-region response for a 12-pulse LFM chirp pulse train with a quadratic phase error. A linear scale is used with truncation at 50% of the peak height.

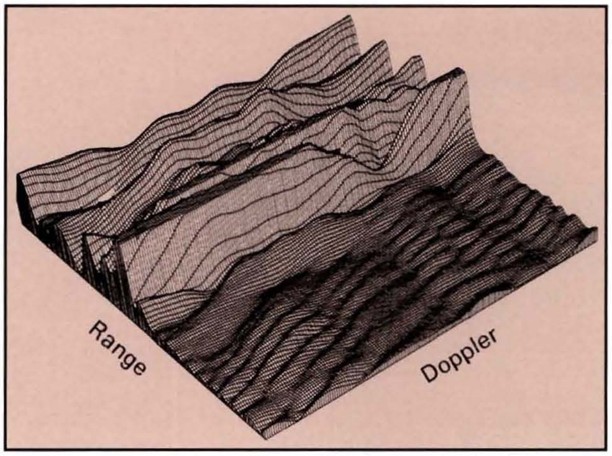

Fig. 28—Ambiguity-function central-lobe-region response for a 12-pulse LFM chirp pulse train with a cubic phase error. A linear scale is used with truncation at 50% of the peak height.

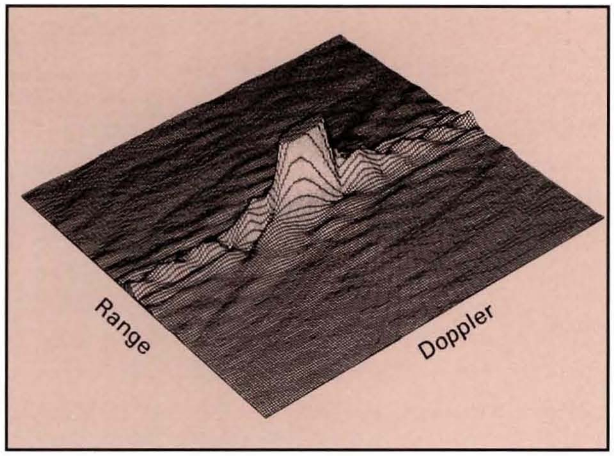

Fig. 29—Ambiguity-function central-lobe-region response for a 12-pulse LFM chirp pulse train with a cubic phase error and with ideal error compensation. A linear scale is used with truncation at 50% of the peak height.

$$\mathbf{y}_d(t) = \varepsilon(t)\mathbf{s}(t)\mathbf{s}^*(t+\Delta)$$
$$= \varepsilon(t)\big|_{\Delta=0}\,.$$

With time alignment Δ to a fraction of the waveform's time resolution, the stretch processor can estimate the complex envelope of the error. The stretch receiver then forms an MF to the corrupted transmit signal.

For example, let us suppose that a simple unmodulated single-pulse waveform is transmitted. Assume that the system introduces a quadratic phase error with an error TB product of 10 across the pulse. Figure 24 shows the ideal response of the single unmodulated pulse, and Fig. 25 shows the MF response without error compensation. Figure 26 shows that the ideally compensated MF response is simply the range-Doppler ambiguity diagram for a single LFM chirp pulse with a TB product of 10.

Now suppose that a 12-pulse LFM chirp pulse train is transmitted, and the TB product for each pulse is 100. Assume that the system introduces a cubic phase error with an error TB product of 10 across each pulse. Further assume that each pulse is Hamming weighted for low-range sidelobes. Figure 27 shows the ideal range and Doppler response of the central peak of the waveform ambiguity diagram, Fig. 28 shows the central-peak response without error compensation, and Fig. 29 shows the ideally compensated central-peak response. These two examples of classical ambiguity functions illustrate the substantial changes that occur in the system MF response as a result of errors and error compensation.

Summary

The optimal processor for a heterodyne-detection range-Doppler imaging laser radar forms a matched filter (MF) to the transmitted waveform. The image range and Doppler resolution is determined by the transmitted waveform's bandwidth and coherence time, respectively. The Doppler, or cross-range, image resolution is shown to be limited by the waveform coherence time and by the target's rotational rate. The statistics of the local-oscillator shot-noise-limited MF output are controlled by atmospheric turbulence and target speckle. Incoherent averaging of successive images is needed to overcome the limits of speckle and atmospheric turbulence.

Two MF imaging technique were presented: ambiguity-function-like (ALF) and subaperture-ambiguity-function-like (SAFL) imaging. The SAFL technique is strictly for periodic pulse train waveforms; the AFL technique is generally applicable to all waveform types. AFL images have point-target responses that are equivalent to the ambiguity function; the point-target response of an SAFL image is given by the central-lobe region of the waveform's ambiguity diagram. The biphase shift-keyed pulse train waveform was shown to have ambiguity-function performance superior to that of the unmodulated pulse and linear frequency-modulated chirp pulse train waveforms in terms of resolution, range-sidelobe level, and Doppler ambiguities. SAFL range-Doppler images of test targets and a single AFL image from stretch-processed data taken at the Firepond indoor test range were presented. Image-enhancement techniques including zero padding, Hamming amplitude weighting, and incoherent averaging were illustrated.

The stretch processor performs matched filtering over a limited range window, or relative delay region, between the received signal and the reference signal. The stretch processor is able to process very wideband LFM chirp waveforms by trading off range windows for processing bandwidth. An all-digital processor has advantages in terms of flexibility to process a wide variety of waveforms without sacrificing the range window, but requires very high-bandwidth A/D converters and real-time array processing capability. The effect of amplitude and phase errors in the transmitted waveform and in the waveform processor is primarily to reduce the dynamic range of the image by increasing the range- and Doppler-sidelobe levels. A simple error-compensation scheme can significantly improve the image quality.

Acknowledgments

The author would like to thank David Nordquist, Alan Stein, and Michael Reiley for their help in producing the range-Doppler images of the Firepond test targets; Neville Harris, who built the wideband single-sideband electro-optic modulator; and David Kocher, James Daley and others at Firepond who built the receiver and signal processor and collected the measurement data.

References

1. A.L. Kachelmyer, "Range-Doppler Imaging: Waveforms and Receiver Design," *SPIE* **999**, 138 (1988).
2. A.L. Kachelmyer, "Coherent Laser Radar Performance in the Presence of Random and Systematic Errors," *SPIE Proceedings* **999**, 176 (1988).
3. J.H. Shapiro, B.A. Capron, and R.C. Harney, "Imaging and Target Detection with a Heterodyne-Reception Optical Radar," *Appl. Opt.* **20**, 3292 (1981).
4. A.L. Kachelmyer, R.E. Knowlden, and W.E. Keicher, "Effect of Atmospheric Distortion of Carbon Dioxide Laser Radar Waveforms," *SPIE* **783**, 101 (1987).
5. A.E. Siegman, "The Antenna Properties of Optical Heterodyne Receivers," *Appl. Opt.* **5**, 1588 (1966).
6. R.M. Gagliardi and S. Karp, *Optical Communications*, (Wiley & Sons, New York, 1976).
7. J.H. Shapiro, "The Target-Reflectivity Theory for Coherent Laser Radars," *Appl. Opt.* **21**, 3398 (1982).
8. F.K. Knight, S.R. Kulkarni, R.M. Marino, and J.K. Parker, "Tomographic Techniques Applied to Laser Radar Reflective Measurements," *Lincoln Laboratory J.* **2**, 143 (1989).
9. M.I. Skolnik, *Radar Handbook*, (McGraw-Hill, New York, 1970), chap. 3, p. 12.
10. F.J. Harris, "On the Use of Windows for Harmonic Analysis with the Discrete Fourier Transform," *Proc. IEEE* **66**, 51 (1978).

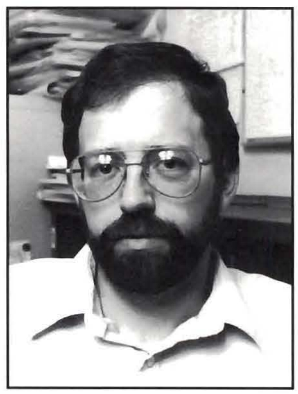

ALAN L. KACHELMYER is a staff member in the Laser Radar Measurements group. He received a B.S. from the University of Minnesota, an M.S. from Syracuse University, and a Ph.D. from the University of Minnesota, all in electrical engineering. From 1973 to 1976 he was with the General Electric Company, Heavy Military Electronics Division, in Syracuse, New York, engaged in radar system theory and design. He did Ph.D. thesis research in the area of communications theory with emphasis on multiuser single-channel decision-feedback equalization systems. In 1979 he joined Lincoln Laboratory and worked on the design of spread-spectrum communication systems with emphasis on data modulation, spreading modulation, security, and error-correction coding schemes. From 1983 to 1985 he worked for Lincoln Laboratory as a radar systems engineer at the Kiernan Re-Entry Measurement Site in the Marshall Islands. Since 1985 he has participated in the development of the Firepond wideband CO_2 range-Doppler imaging laser radar. His current research interests include waveform design, signal processing, passive and active tracking, image signal processing, and other laser radar system issues.